RESERVOIR FLUID AND ROCK CHARACTERIZATION OF A PERUVIAN OIL RESERVOIR

A Thesis

by

DAVID ALEJANDRO HIGUERA BARRERO

Submitted to the Office of Graduate and Professional Studies of
Texas A&M University
in partial fulfillment of the requirements for the degree of

MASTER OF SCIENCE

Chair of Committee,	Hadi Nasrabadi
Co-Chair of Committee,	Akhil Datta-Gupta
Committee member,	Sara Abedi
Head of Department,	Duane A. McVay

May 2018

Major Subject: Petroleum Engineering

ABSTRACT

In this study, a reservoir fluid and rock characterization is done for a Peruvian oil reservoir.

A robust workflow for validation of laboratory *PVT* work is applied. This approach was originally proposed by Professor William D. McCain, Jr. at Texas A&M University. No practical applications of it have been published before.

The reservoir rock characterization was done by definition of hydraulic flow units from core data. A traditional method of analysis, which uses a subjective judgment regarding the number of flow units and their corresponding limits, was enhanced by use of hierarchical cluster analysis. This implementation was done in the form of a MATLAB code. The algorithm automatically determined the optimum number of flow units and their associated limits. It is noteworthy to clarify that hierarchical cluster analysis for hydraulic flow unit definition has been proposed earlier. However, this study provides a clearer guidance on how to use it appropriately. Cluster calibration was done by integration of rock-fluid properties, as distinct relative permeability and capillary pressures exist for each flow unit.

DEDICATION

To my wife, Paola, and my daughter, Valentina, who is most precious gift of my life.

ACKNOWLEDGEMENTS

I would like to thank my committee chair, Dr. Hadi Nasrababi, committee co-chair Dr. Akhil Datta-Gupta and committee member Dr. Sara Abedi.

I am also grateful for the financial support provided by the Texas A&M Engineering Experiment Station (TEES) and by Zeus OL Peru SAC, formerly known as Sechura Oil and Gas and Olympic Perú.

Thanks also go to my friends and colleagues and the department faculty and staff for making my time at Texas A&M University an unforgettable experience.

I am especially thankful to the following faculty members for their guidance and support throughout my journey at Texas A&M University: Dr. I. Yucel Akkutlu and Dr. John Lee, whom I was honored to meet.

Finally, I would like to thank my wife Paola for her lovely support, and for joining me in this extraordinary adventure. She has been my constant inspiration and motivation.

CONTRIBUTORS AND FUNDING SOURCES

This work was supported by a dissertation committee consisting of Dr. Hadi Nasrababi and Dr. Akhil Datta-Gupta of the Department of Petroleum Engineering, and Dr. Sara Abedi of the Departments of Petroleum Engineering and Civil Engineering.

The data analyzed throughout this thesis was provided by the company Zeus OL Peru SAC, formerly known as Sechura Oil and Gas and Olympic Perú.

All other work conducted for the thesis was completed by the student independently.

This work was made possible in part by funding contributions from the Texas A&M Engineering Experiment Station (TEES) and Zeus OL Peru SAC.

NOMENCLATURE

B	Formation volume factor
C_n	Average *FZI* value for a given cluster *n*
c_o	Oil compressibility
E_{Dmax}	Displacement efficiency at residual oil saturation
F_s	Shape factor
h	Thickness
k	Permeability (horizontal)
k_r	Relative permeability
k_j	Equilibrium ratio, or *k*-factor, of component *j*
m	Original reservoir gas cap volume to original reservoir oil volume ratio
P	Pressure
P_c	Capillary pressure
Pc_j	Critical pressure of component j
R_{SB}	Solution gas-oil ratio at the bubble point pressure
R_{SP}	Producing gas-oil ratio from the separator
R_{ST}	Producing gas-oil ratio from the stock tank
S_{gv}	Surface area per unit grain volume
S_g	Gas saturation
S_{gcr}	Critical gas saturation
S_w	Water saturation
S_{wir}	Irreducible water saturation

S_{orw}	Residual oil saturation after waterflood
S_{org}	Residual oil saturation after an immiscible gas flood
T	Temperature
T_{Bj}	Normal boiling point of component j
Tc_j	Critical temperature of component j
V/V_{sat}	Relative oil volume in a Constant Composition Expansion (*CCE*) test
x_j	Molar compositions of component j in the liquid at equilibrium
y_j	Molar compositions of component j in the gas at equilibrium

Greek Symbols

ϕ	Porosity
ϕ_z	Void ratio
τ	Tortuosity
ρ_a	Apparent liquid density
ρ_{oRb}	Reservoir oil density at the bubble point
ρ_{STO}	Stock-tank oil density at standard conditions
γ_g	Weighted average specific gas gravity
γ_{gSP}	Separator gas specific gravity
γ_{gST}	Stock-tank gas specific gravity
γ_{STO}	Stock-tank oil specific gravity
$\Delta\rho_p$	Pressure correction in fluid property correlations
$\Delta\rho_T$	Temperature correction in fluid property correlations
λ_{rt}	Total relative mobility

Subscripts

b	Bubble point
i	Initial conditions
R	Reservoir conditions

Abbreviations

AARE	Average absolute relative error
API	American Petroleum Institute
FZI	Flow Zone Indicator
NTG	Net to gross ratio
RB	Reservoir barrel, or barrel at reservoir conditions
RQI	Rock Quality Index
SSE	Sum of squared errors
TVDss	True vertical depth from the sea level to the point of interest

Units

°F	Fahrenheit degrees
cp	Centipoise
ft	Feet
lb/ft^3	Pounds (mass) per cubic feet
psia	Pounds (force) per square inch (absolute pressure)
SCF	Cubic feet measured at standard conditions
STB	Barrel measured at standard conditions

TABLE OF CONTENTS

Page

LIST OF FIGURES

Page

LIST OF TABLES

Page

CHAPTER I

INTRODUCTION

1.1 Statement of the Problem

Production from an oil field located in northern Perú started in 2007. Within 6 years of production, the reservoir pressure dropped to almost 10% its initial value, resulting in a steep production decline. In 2015, a waterflooding pilot project was started. Although initial results were promising, the subsequent field wide implementation of the project has not met the operator's expectations. Injected water breakthrough has occurred earlier than expected and incremental oil is less than the anticipated volume. A reservoir (rock and fluid) characterization was done to better understand the displacement process. Leading industry-proven techniques were applied.

1.2 Research Outline

Rock and fluid characterization of a Peruvian oil field is presented in Chapter II and Chapter III.

Chapter II presents the reservoir fluid characterization. The primary objective of this chapter is to introduce representative pressure-volume-temperature (*PVT*) relationships and relevant associated fluid properties. Lack of actual *PVT* samples taken at early stages of field development made impossible to establish such relationship in the laboratory. Thus, well logs, production and pressure data, analog *PVT* samples and fluid property correlations were used.

Chapter III depicts the reservoir rock characterization. The primary objective of this chapter is to describe the reservoir rock in terms of hydraulic flow units (*HFU*). Such representation was done by means of the flow zone indicator (*FZI*) and rock quality index (*RQI*)

parameters. This approach, originally proposed by Amaefule *et al* [1993], was combined with hierarchical cluster analysis to objectively determine the optimum number of *HFU* and their corresponding *FZI* values in a way similar to that presented by Abbaszadeh *et al* [1996] and Dezfoolian *et al* [2013]. The approach proposed in this thesis differs from the latest in at least two ways. First, the absolute error measurement of each cluster is replaced by a relative error measurement. Secondly, the similarity measurement is defined as the L_1 norm (i.e. city block or Manhattan distance).

1.3 Field Case Description

All methods and analysis presented here were applied to an oil field located in northern Perú. Main producing formation is locally named *Salinas* (Eocene). **Figure 1.1** shows a structural map on top of the formation along with the bottomhole position of the wells. There are 40 wells in total. Production started in 2007 and within 6 years the reservoir pressure had dropped to almost 10% its initial value. The severe pressure depletion resulted in a steep production decline.

In 2015, a waterflooding pilot project was started, and by 2018 there were 7 water injectors. Repressurization by water injection from reservoir pressures lower than the bubble point pressure (P_b) would have resulted in a collapsing gas saturation, and implies a situation of repressurization under variable bubble point pressure.

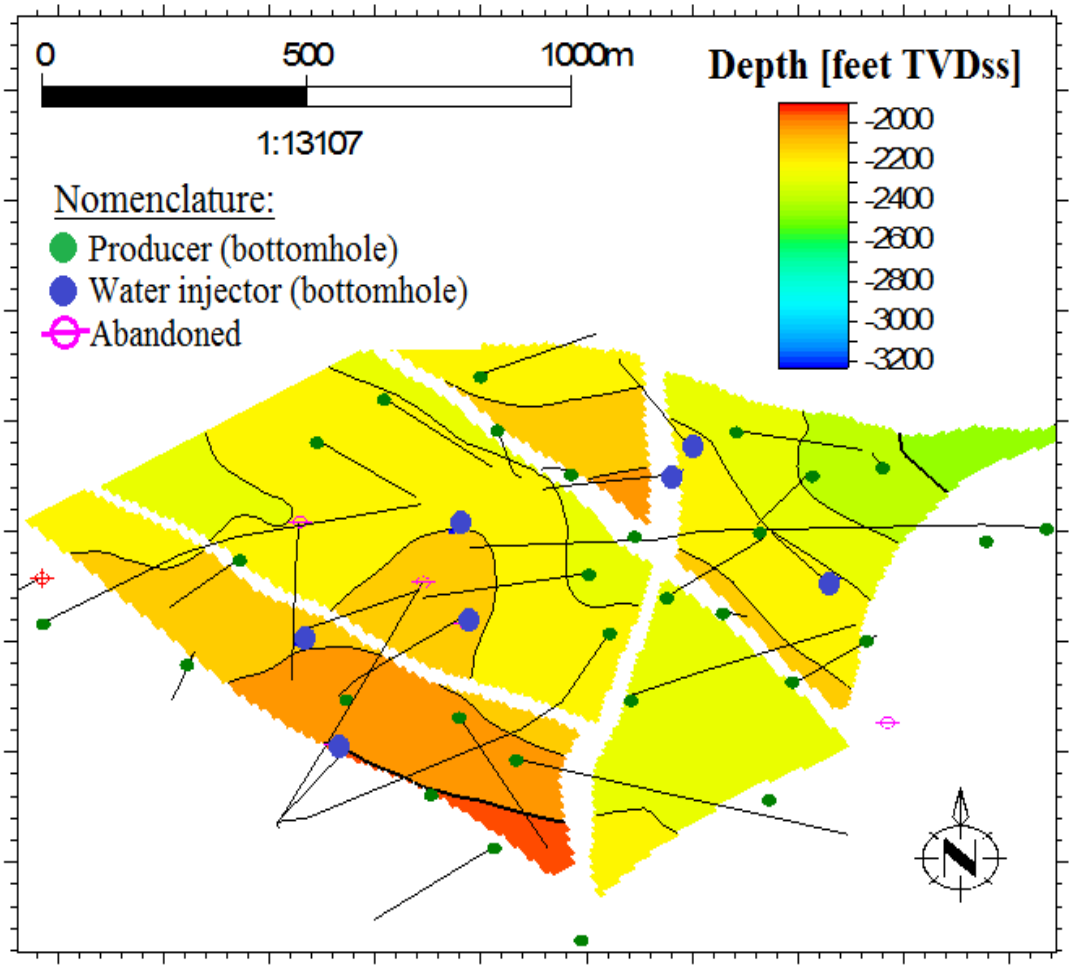

Figure 1.1 Wells and structural configuration of the reservoir on top of the formation

The producing formation is found at a depth interval ranging from -2,000 to -3,000 ft TVDss. A unique oil-water contact (*OWC*) is found at -2,800 ft TVDss.

The reservoir is initially undersaturated.

Table 1.1 summarizes relevant average rock and fluid properties. Although some of this data is calculated in later chapters, it is convenient to present it upfront.

Table 1.1 Reservoir and fluid properties

Reservoir Properties:		
Gross thickness, h	=	1,000 ft
Estimated net to gross ratio, NTG	=	0.53
Average porosity, ϕ	=	0.109 (fraction)
Average irreducible water saturation, S_{wirr}	=	0.767 (fraction)
Average permeability, k	=	8.9 md
Average depth to reservoir top	=	-2,000 ft TVDss
Average depth to reservoir base	=	-3,000 ft TVDss
Original oil-water contact, OWC	=	-2,800 ft TVDss
Fluid Properties:		
API gravity, $°API$	=	42
Bubble point pressure, P_b	=	1,526 psia
Oil formation volume factor at P_i, B_{oi}	=	1.1496 RB/STB
Oil viscosity at P_i, μ_{oi}	=	1.5426 cp
Solution gas-oil ratio at P_i, Rs_i	=	326 SCF/STB
Oil compressibility at P_i, c_{oi}	=	9.17×10^{-6} psi^{-1}
Additional Information:		
Initial reservoir pressure, P_i	=	1,785 psia
Datum depth	=	-2,500 ft TVDss
Original gas cap to oil reservoir volume ratio, m	=	0 RB/RB

CHAPTER II

RESERVOIR FLUID CHARACTERIZATION

The main challenge for the characterization of the reservoir fluid was the lack of *PVT* laboratory analysis. Uncertainty therefore existed for all fundamental fluid properties such as bubble point pressure (P_b), solution gas-oil ratio at the bubble point (R_{SB}), etc. Other sources of information had to be evaluated. These included well log data, production history, analog fluid *PVT* reports and fluid property correlations.

2.1 Literature Review

If laboratory *PVT* data are not available, published correlations are frequently used for estimation of reservoir fluid properties as a function of pressure. Many correlations have been published for gas, oil and water. McCain *et al* [2011] however, compiled this vast number of correlations and systematically determine their accuracy by comparing their predicted properties with a large set of measured fluid property data. Measured data covered the full range of conditions and properties that might be found in practice. For these correlations to yield a representative description of the reservoir fluid, accurate input parameters, such as bubble point pressure (P_b) and solution gas-oil ratio at the bubble point (R_{SB}) among others, need to be provided.

Examination of field gas oil-ratio (*GOR*) and historical reservoir pressure data is a reliable approach to approximate P_b and R_{SB} as discussed by several authors (Dake [1978], McCain *et al* [2011]). In fact, when laboratory data is available, it is recommended to check P_b and R_{SB} against field pressure and production data (Baker *et al* [2015]). McCain *et al* [2011] however, make an important clarification. Since field measured gas production occurs at the separator (first-stage

separator usually), then estimates of the gas volume vented from the stock tank must be made and added in order to obtain true values of the solution gas-oil ratio at the bubble point pressure (R_{SB}).

Well log data can also be helpful in estimating P_b. In particular, Neutron-Density logs are used in the practice to establish the position of the gas-oil contact (*GOC*). If these logs are run early in the life of a reservoir having an original gas cap, the depth to the original *GOC* can be established. The reservoir pressure corresponding at that depth would equal P_b (Baker *et al* [2015]). For an undersaturated oil reservoir, no gas cap would exist at initial conditions and the Neutron-Density logs would not have a crossover. In this case, no direct estimate of P_b can be made, but an upper limit can be defined as P_b must not be greater than the initial reservoir pressure (measured at any height in the oil column).

Analog *PVT* data is another option if no laboratory analysis were conducted on fluid samples from the actual reservoir. As in the case of any oil *PVT* analysis, representative fluid samples could only be obtained if the reservoir pressure, and the pressure at the bottom of the test well at the time of sampling, do not drop below P_b (Archer *et al* [1986], McCain [1990]). Samples can be obtained either at the surface or downhole. In general, a sample is valid if the gas and liquid are in equilibrium at the time of sampling (Pedersen *et al* [2015] and McCain [2016]).

Not only fluid samples need to be valid for a *PVT* study to be representative. The lab work itself has to be accurate as well. McCain [2016] has proposed a workflow to validate the accuracy of laboratory analysis. He suggests using reliable fluid property correlations, such as those in McCain *et al* [2011], to check the accuracy of laboratory data.

2.2 Field Gas Oil-Ratio

Figure 2.1 shows the historical producing gas-oil ratio from the separator, i.e. R_{SP} or field *GOR* data, and reservoir pressure data. As of early 2008, R_{SP} starts increasing, marking the point in time at which the reservoir pressure drops below P_b. From this data, limiting values of P_b and R_{SP} were defined as follows: 1,400 psia < P_b < 1,785 psia; and 200 SCF/STB < R_{SP} < 600 SCF/STB. Early drill stem test (*DST*) in the field helped defined R_{SP} as 326 SCF/STB.

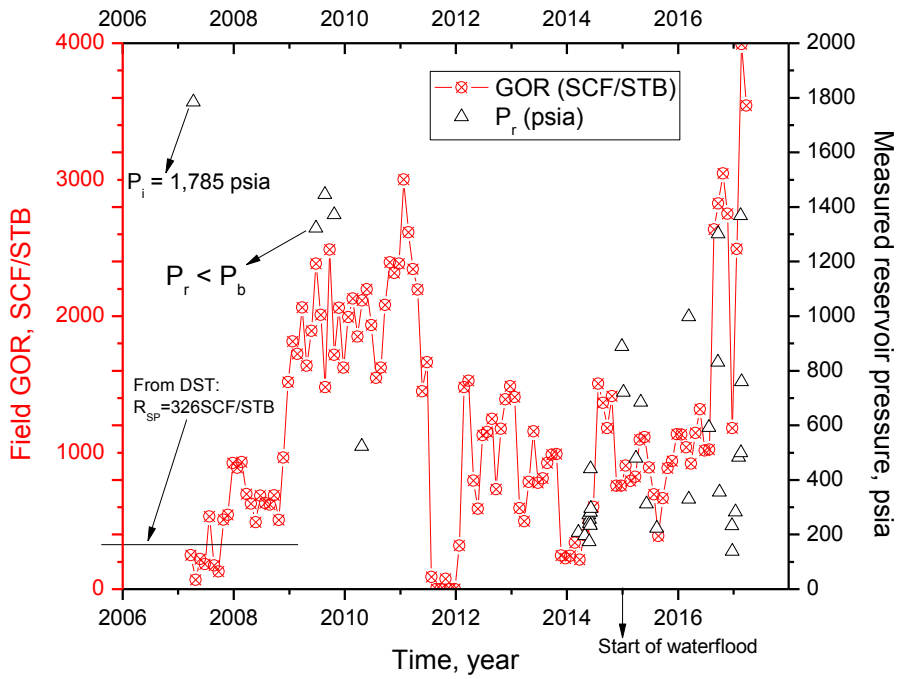

Figure 2.1 Field GOR and reservoir pressure (P_r) history

Two observation are worth making. First, early R_{SP} data in **Figure 2.1** differs from R_{SB} by the amount of gas produced at the stock tank. The producing gas-oil ratio from the stock-tank (R_{ST}) must be added to R_{SP} data if a more precise estimation of R_{SB} is needed. Since in practice R_{ST} is seldom measured, McCain *et al* [2011] recommends to increase R_{SP} by 16.2%. A second observation is that the decrease in R_{SP} in 2011 is not due to water injection, which started in 2015.

This decline is due to the behavior of the gas formation volume factor (B_g) at low pressures, causing B_g to increase more rapidly than the increasing gas relative mobility (Slider [1983]).

2.3 Well Log Data

Well log data also confirmed the reservoir was originally subsaturated and help constraining P_b. Figure 2.2 shows well logs data in 5 wells located high in the reservoir structure. Of particular interest is Well 3, which was drilled early in the life of the reservoir and showed no indications of an original gas cap. Additionally, during drill stem test (*DST*) operations the well flowed oil and gas from perforations at the top of the producing formation.

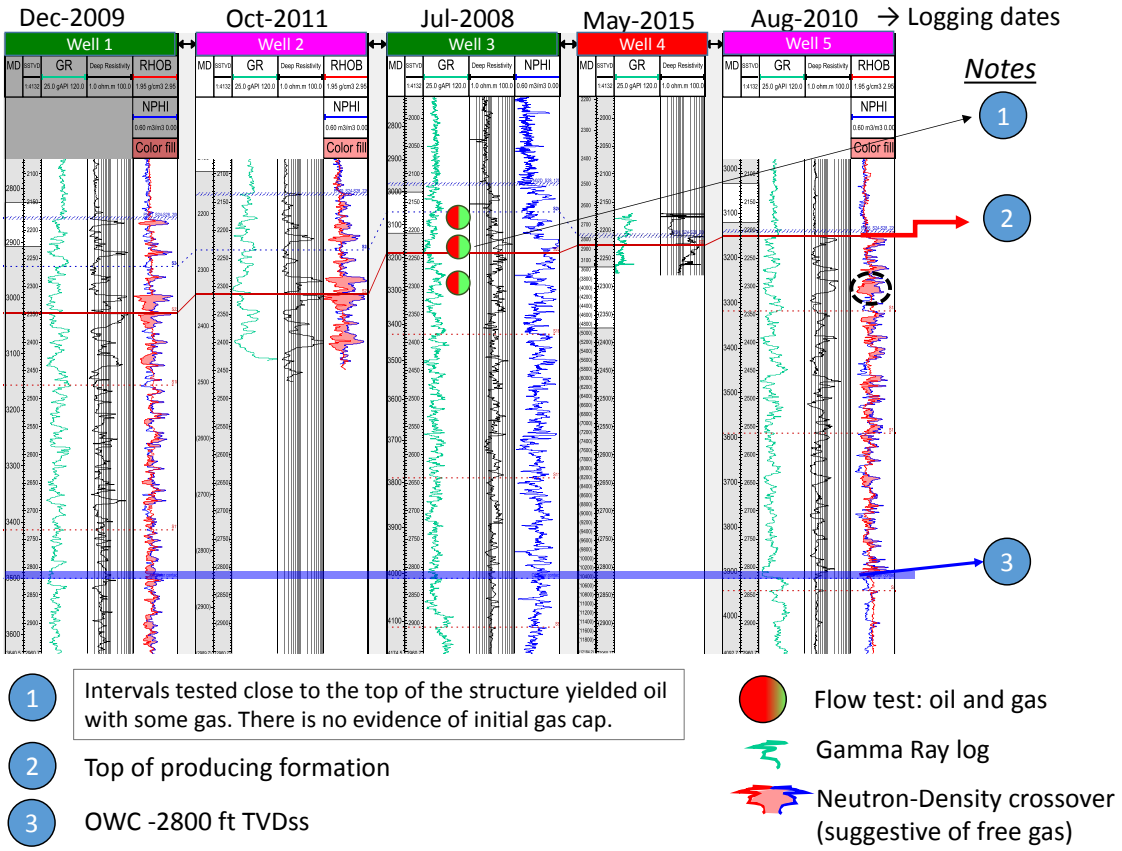

Figure 2.2 Well log data in structurally high wells

The absence of a gas cap at original conditions meant P_b was lower than the reservoir pressure at the top of the structure.

2.4 Analog PVT Data

Three *PVT* studies (i.e. laboratory analysis) done on samples collected from nearby analog reservoirs were available. **Table 2.1** summarizes some relevant data.

Table 2.1 Analog PVT data

Sample number	Sample location	°API	P_b (psia)	Temperature (°F)	R_{SB} (SCF/STB)
1	Separator	35.4	122	122	283
2	Downhole	43.6	119	119	357
3	Downhole	39.5	118	118	389

Validation of analog *PVT* information was done in two steps: first, vapor-liquid equilibrium (*VLE*) at the time of sampling was checked to determine the validity of the samples; and secondly, the lab work itself was validated through the method proposed by McCain [2016]. The workflow is presented in detail in **Figure 2.3**. Validation of fluid samples can only be attempted for surface (i.e. separator) samples though, and no method exists in the industry to validate downhole samples (McCain [2016]).

Additional details on the workflow depicted in **Figure 2.3** are presented in the next two sections.

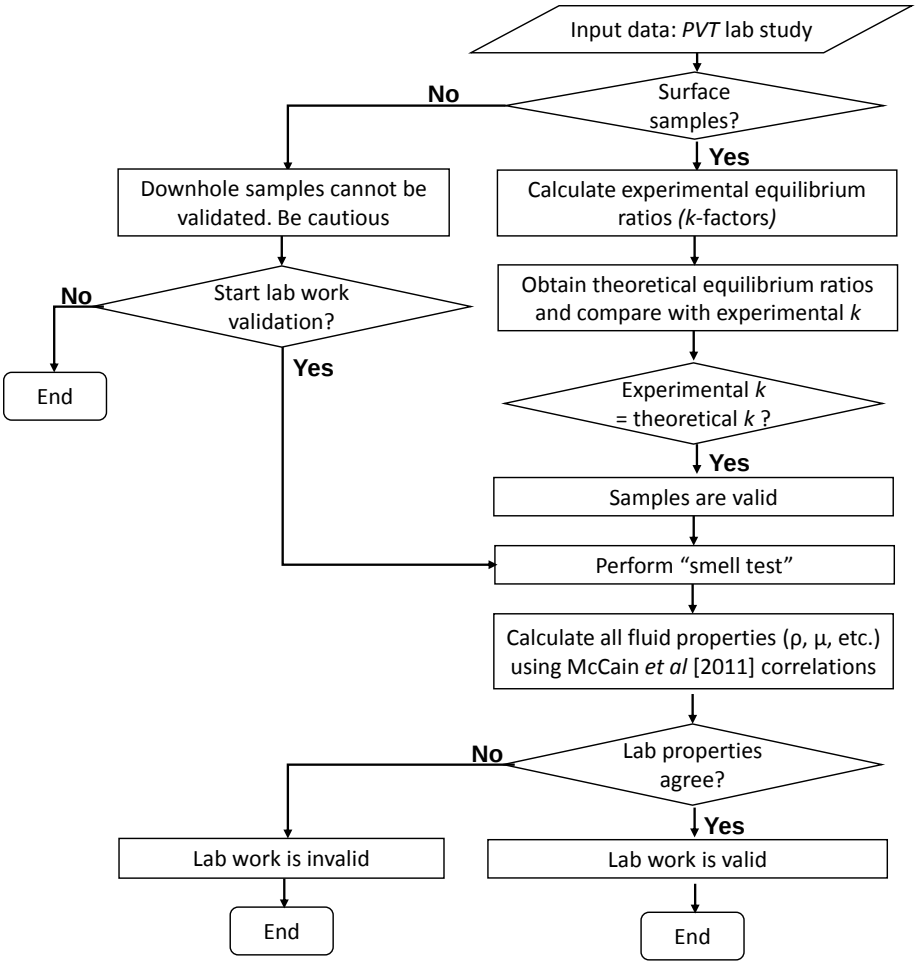

Figure 2.3 Workflow proposed by McCain [2016] for validation of fluid samples and *PVT* laboratory analysis

2.4.1 Validation of fluid samples

For surface (i.e. separator) fluid samples to be valid for further *PVT* laboratory analysis, the sampled separator gas and separator liquid must be in equilibrium (McCain *et al* [2016] and Pedersen *et al* [2015]). At equilibrium conditions, the separator gas is at its dew point and the separator oil at its bubble point. This means that the phase envelopes of the separator gas and separator liquid have a point of intersection at the separator conditions (Pedersen *et al* [2015]). **Figure 2.4** illustrates this point.

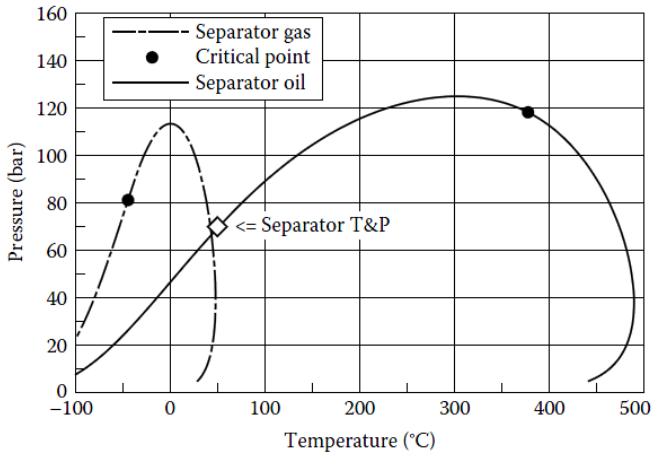

Figure 2.4 Phase envelopes of a separator gas and separator oil (after Pedersen *et al* [2015])

A reasonably accurate way to predict vapor-liquid equilibrium (*VLE*) is through correlations based on experimental observations of *VLE* behavior (McCain [1990]). These correlations, such as Bruno *et al* [1972], invoke use of equilibrium ratios, or *k*-factors, for the different components in a mixture. For a component *j*, its *k*-factor is defined as follows:

$$k_j = \frac{y_j}{x_j} \tag{2.1}$$

Where y_j and x_j are the gas and liquid compositions respectively that exist at equilibrium at a given pressure and temperature. These compositions are given as mole fractions, and are experimentally determined.

Theoretically derived *k*-factors, using the correlation by Bruno *et al* [1972], were compared against experimental *k*-factors to assess the quality of fluid samples. Agreement between the two would exist if the sampled gas and liquid are in equilibrium (Pedersen *et at* [2015] and McCain [2016]). Pressure and temperature conditions are those prevailing at the separator for surface fluid samples. **Figure 2.5** is such a plot for the analog surface fluid sample. In this plot, *k*-factors

correspond to a pressure and temperature of 45 psig and 90 °F, which were the reported sampling conditions. In this plot, the abscissa is the Hoffman, Crump & Hocott (*HCH*) plotting function defined by Hoffman *et al* [1953] as:

$$HCH = \left[\frac{\log(P_{Cj}) - \log(14.7)}{\frac{1}{T_{Bj}} - \frac{1}{T_{Cj}}}\right]\left[\frac{1}{T_{Bj}} - \frac{1}{T}\right] \tag{2.2}$$

Where P_{Cj} and T_{Cj} are the critical pressure and critical temperature, T_{Bj} is the normal boiling point and T is the prevailing temperature. All pressures and temperatures are in absolute quantities.

The linear trend of the experimental *k*-factors in **Figure 2.5** suggested the sampled gas and liquid were in equilibrium. However, the disagreement with the theoretical *k*-factors implied the samples were in equilibrium at conditions other than those reported.

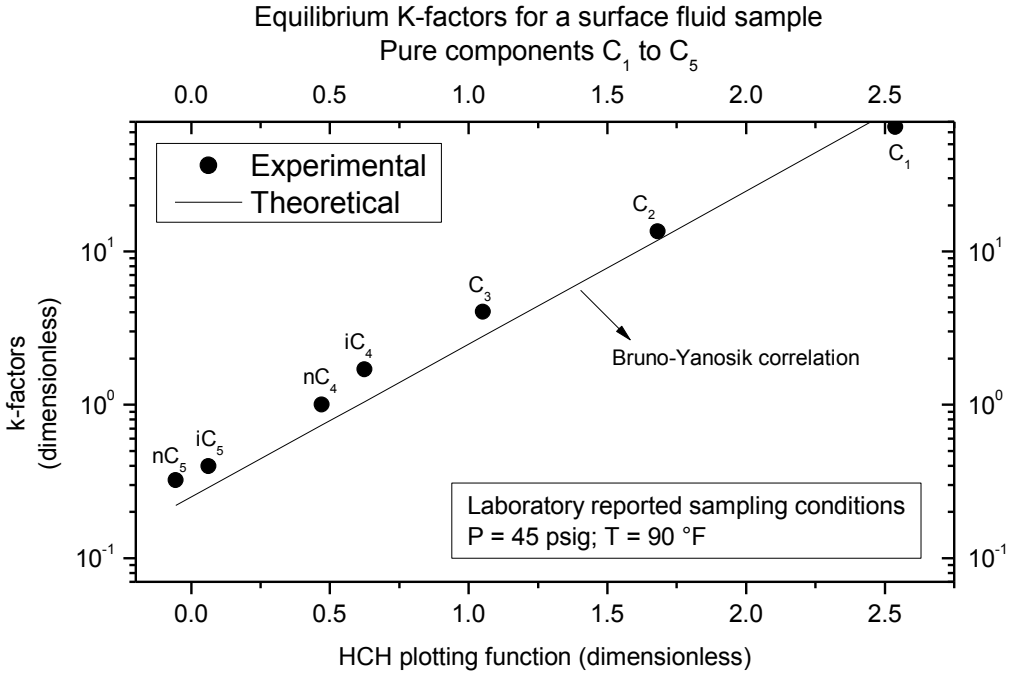

Figure 2.5 Experimental and theoretical *k*-factors against the Hoffman, Crump & Hocott plotting function at reported separator pressure and temperature: assessment of equilibrium for analog oil and gas surface samples

The theoretical *k*-factors were recalculated at a separator pressure and temperature of 45 psig and 110 °F. Figure 2.6 plots the data. Agreement between experimental and theoretical *k*-factors suggests these were the likely actual equilibrium conditions.

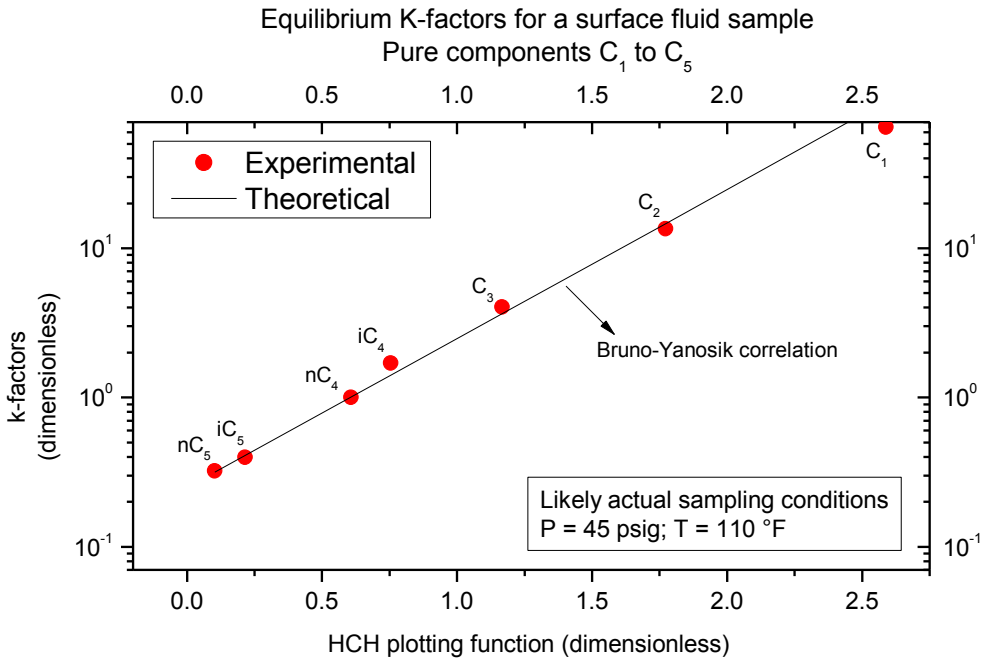

Figure 2.6 Experimental and theoretical k-factors against the Hoffman, Crump & Hocott plotting function at likely actual separator pressure and temperature: assessment of equilibrium for analog oil and gas surface samples

In **Figures 2.5** and **2.6** the only components shown are C_1 thorough n-C_5 because the compositional analysis did not discriminate higher molecular weight isomers.

Based on the previous analysis, the analog surface fluid sample was considered valid. On the other hand, the validity of the downhole samples remained unknown, as this analysis is not applicable.

The next stage in the workflow (**Figure 2.3**) was to validate the laboratory work itself.

2.4.2 Validation of laboratory work

This section includes a direct field application of a robust workflow to validate laboratory work proposed by Professor William D. McCain, Jr. at Texas A&M University (McCain [2016]). He proposes a two-step approach. First, an overall quality check of the laboratory report is done, and visible inconsistencies are determined by a limited number of calculations. This step was named "*smell test*". Secondly, reliable fluid property correlations, such as those in McCain *et al* [2011], are used to check the accuracy of laboratory data.

A quality check done during the "*smell test*" involves use of the following equation:

$$B_{ob} = \frac{\rho_o + 0.01357 R_{SB} \gamma_g}{\rho_{oRb}} \tag{2.3}$$

Where B_{ob} and ρ_{ob} are the oil formation volume factor and oil density at the bubble point in RB/STB and lb/ft^3 respectively, and γ_g is the weighted average gas specific gravity. **Equation 2.3** is not a correlation, but the result of a material balance (McCain *et al* [2011]).

In short, the "*smell test*" was perform on all three samples and no inconsistencies were found. For example, application of **Equation 2.3** to the data from differential liberation tests and separator tests revealed a difference of about 2% in most cases.

Next, relevant fluid properties were calculated using the correlations by McCain *et al* [2011]. They are reproduced from McCain *et al* [2011] in Appendix A. Input parameters for these correlations were laboratory R_{ST} and R_{SP} from the separator test; *API* gravity; laboratory separator gas and stock-tank gas specific gravities (γ_{gSP} and γ_{gST}); and temperature of the laboratory *PVT* cell.

Table 2.2 shows the deviations of the correlations from the experimental data. As observed, the highest deviation occurs for the oil viscosity. This is most likely because among all property correlations presented by McCain *et al* [2011], the oil viscosity is the least accurate correlation. In fact, the average absolute relative errors shown in **Table 2.2** fall within those reported by McCain *et al* [2011]. Thus, in the case of oil viscosity alone, fluid correlations cannot be use to validate laboratory work.

In **Table 2.2**, V/V_{sat} is the relative volume in the Constant Composition Expansion[1] (*CCE*) tests. Other properties not shown in **Table 2.2**, such as the isothermal compressibility, can be derived from the properties used as input for the correlations and those in the table.

Table 2.2 Average absolute relative error between fluid property correlations in McCain *et al* [2011] and experimental *PVT* data

		Laboratory report number in Table 2.1		
Property	**Relative error**	**No.1**	**No.2**	**No.3**
ρ_o	minimum	0.39%	0.22%	0.45%
	average	0.67%	0.48%	0.62%
	maximum	0.88%	0.67%	0.70%
V/V_{sat}	minimum	0.00%	0.03%	0.01%
	average	0.03%	0.04%	0.07%
	maximum	0.07%	0.05%	0.13%
B_o	minimum	0.11%	0.00%	0.00%
	average	0.21%	0.46%	0.49%
	maximum	0.48%	0.69%	0.71%
μ_o	minimum	1.78%	8.88%	2.23%
	average	13.51%	36.53%	29.01%
	maximum	39.28%	47.92%	51.76%

[1] In a *CCE* test, the oil relative volume is defined as the ratio of the volume of a given mass of oil at a pressure greater than the bubble point to the volume of the same mass at the bubble point.

The error metric presented in **Table 2.2** is the average absolute relative error (*AARE*). For *n* measurements at *n* different pressures of an experimental variable (y_{exp}), the average deviation of a correlated variable y_{cor} is defined as:

$$AARE = \frac{100}{n}\sum_{i=1}^{n}\left|\frac{y_{cor}-y_{exp}}{y_{exp}}\right| \tag{2.4}$$

Equation 2.4 is the same error metric used by McCain *et al* [2011].

Given the small *AARE* values in **Table 2.2**, and following the proposed approach by Professor William D. McCain, Jr., the analog *PVT* laboratory work was considered valid.

2.5 Reservoir Fluid Model

Validated analog *PVT* data and fluid property correlations were combined together to yield a description of the reservoir fluid that suits the actual reservoir temperature, *API* gravity and estimated R_{SB} from production data (**Table 1.1**). Specifically, correlations by McCain *et al* [2011] were used to estimate all gas and oil properties. These correlations are reproduced in Appendix A. In the case of oil viscosity however, analog *PVT* data was used alone, as it is more representative of this reservoir fluid than fluid correlations. Input parameters for these correlations, such as solution gas-oil ratio at the bubble point (R_{SB}), were estimated from production data and field measurements.

Figure 2.7 presents the resulting oil *PVT* data. Data depicted in this figure corresponds to a fixed bubble point pressure case. The fluid model is black-oil, meaning all changes in the system are determined mainly as a function of pressure (Wattenbarger [2000]). In **Figure 2.7** all properties are given at a fixed reservoir temperature of 115 °F.

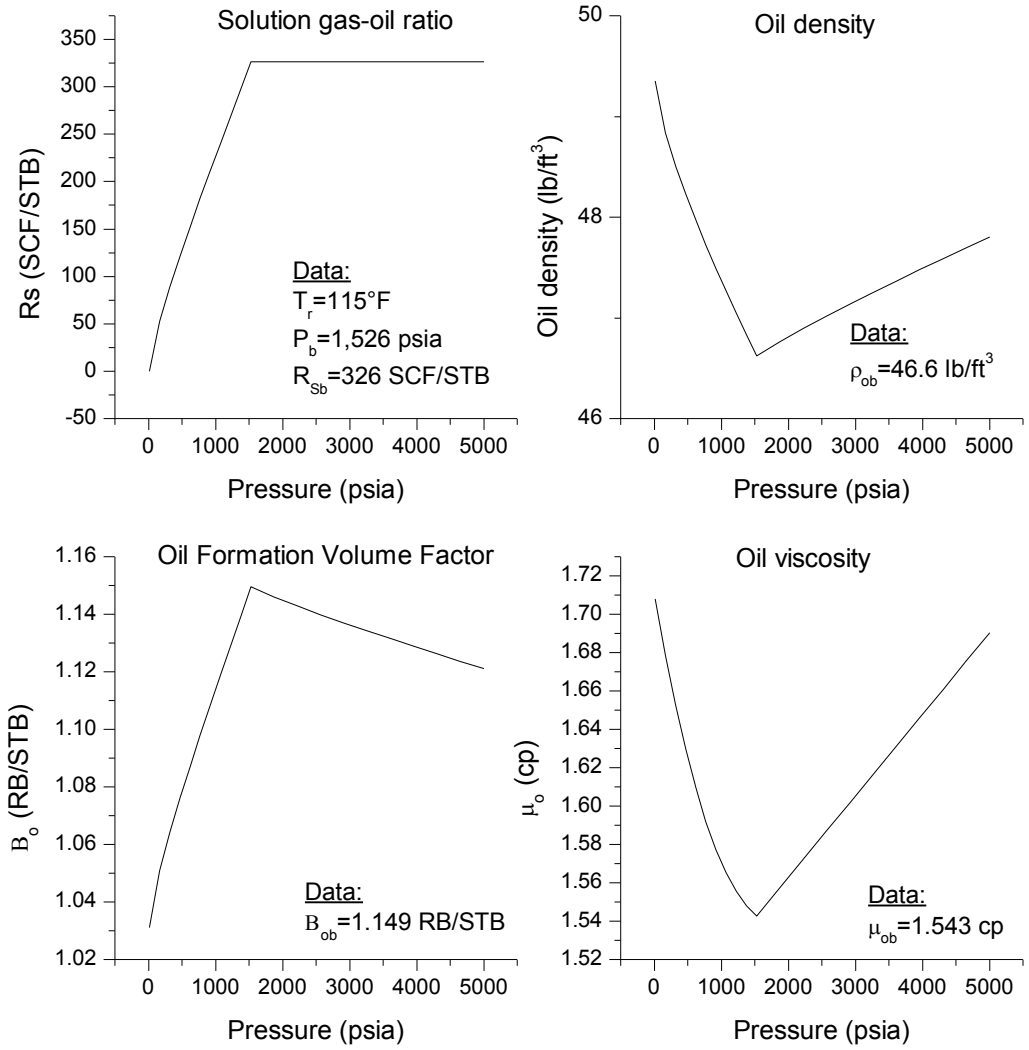

Figure 2.7 Oil PVT model: fixed bubble point case

The fixed bubble point case however, would not accurately represent this reservoir. As mentioned before, the reservoir was produced from 2007 to 2015 under pressure depletion, and the reservoir pressure dropped to almost 10% its initial value. At that point in time a waterflooding project was started, and repressurization was observed (**Figure 2.1**). The process involves repressurization under variable bubble point pressure as the bubble point would depend on the

available gas. In fact, waterfloods applied to saturated oil reservoirs frequently cause the gas saturation in regions near the injectors to reduce to zero at pressures below the original bubble point (Wattenbarger [2000]).

Figure 2.8 presents the variable bubble point oil *PVT* model. Each line in this figure represents undersaturated data with different solution gas-oil ratios, and thus different bubble points. As shown in **Figure 2.8**, data has been extrapolated above the original bubble point pressure. This is required for an accurate representation of repressurization processes with variable bubble point (McCain and Spivey [1999] and Wattenbarger [2000]). Consistencies of oil and gas properties were checked by ensuring that the oil compressibility (c_o) remains positive throughout the range of extrapolated pressure. The formal definition of c_o is given by **Equation 2.5**.

$$c_o = -\frac{1}{B_o}\left[\left(\frac{\partial B_o}{\partial P}\right)_T - B_g\left(\frac{\partial R_s}{\partial P}\right)_T\right] \tag{2.5}$$

Thus, for c_o to remain positive and pass the compressibility check, the following inequality must be satisfied (McCain and Spivey [1999]):

$$\Delta B_o < B_g \Delta R_s \tag{2.6}$$

In **Equation 2.6**, the value of the gas formation volume factor (B_g) is determined at the lower pressure.

Additionally, in **Figure 2.8** the maximum pressure along the abscissa has also been increased to ensure that at all times and for all gridblocks, the simulator will interpolate, rather than extrapolate, the *PVT* data.

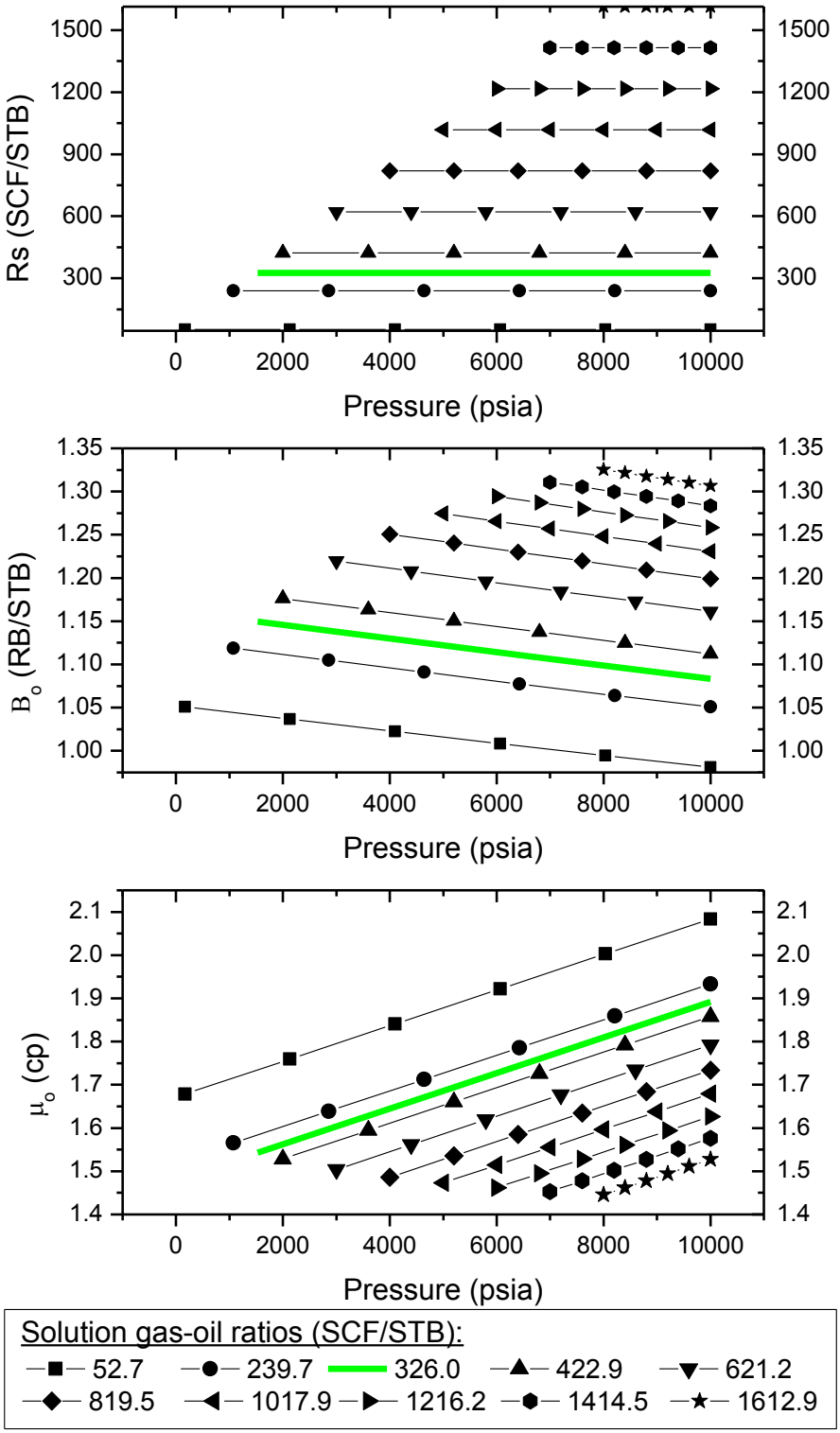

Figure 2.8 Oil *PVT* model: variable bubble point case. Green lines reproduce the oil properties previously shown in the fixed bubble point case

2.6 Summary

Lack of *PVT* data from actual fluid samples was overcome by means of analog *PVT* data and reliable fluid property correlations. Input parameters for these correlations, such as solution gas-oil ratio at the bubble point (R_{SB}), were estimated from production data and field measurements. Analog *PVT* data was validated beforehand by comparison of experimental and theoretical equilibrium ratios, or *k*-factors, and through the application of a robust workflow originally proposed by Professor William D. McCain, Jr. at Texas A&M University (McCain [2016]).

The resulting fluid model is a black-oil variable bubble point model, in which internal consistencies of gas and oil properties were checked by ensuring that the oil compressibility (c_o) remains positive throughout the range of extrapolated pressure.

CHAPTER III

RESERVOIR ROCK CHARACTERIZATION

Characterization of the reservoir rock is required for proper representation of rock properties in a tridimensional model. The underlying challenge is to identify relationships between the observed rock properties in core samples, and then use those relationships to predict permeability, and other rock properties, in uncored wells.

3.1 Literature Review

Estimation of permeability in uncored, but logged, wells has been a generic problem common to all reservoirs. Therefore, procedures and methods have been sought to allow property estimation at these locations. Traditional approaches include simple linear regressions between core porosity and the logarithm of core permeability. Then, these regressions are applied to uncored wells given some inference of porosity from log data.

More accurate predictions of permeability can be achieved by addressing the development of permeability in porous rocks from fundamental concepts of geology and flow through porous media (Abbaszadeh *et al* [1996]). Specifically, the intent is to define functional relationships for permeability based on pore-throat geometry parameters. This is best achieved by identifying and grouping portions of rock within the reservoir having similar fluid conductivity. These groups are known as hydraulic flow units (*HFU*).

Earlier definitions of *HFU* were provided by Bear [1972] and Ebanks [1987]. They defined a *HFU* as a body of rock in which geological and petrophysical properties related to the flow of fluids are consistent and predictably different from properties of other *HFU*.

Several methods have been proposed in the literature for rock characterization based on *HFU*. Stolz and Graves [2003] provides a summary of some of them. Notably, there is no universally applicable method.

One of the most widely used methods was proposed by Amaefule *et al* [1993]. The method, which is based on the Kozeny-Carman equation (Carman [1961]), defines a characteristic parameter for each *HFU* named flow zone indicator (*FZI*). In the original work by Amaefule *et al* [1993], *FZI* values were determined graphically, in which was later known as graphical clustering. Graphical clustering of *HFU* is subjective, since the number of flow units, and their corresponding limits, are not uniquely determined. A solution was later given by Abbaszadeh *et al* [1996]. They proposed to use the Ward' algorithm, an analytical technique in hierarchical cluster analysis, to objectively evaluate *HFU*. Their work significantly advanced the method. However, the number of cluster, i.e. *HFU*, in the Ward's algorithm was an input, and therefore the evaluation still suffered from subjectivity. Later on, other authors, such as Svirsky *et al* [2004] and Dezfoolian *et al* [2013], adopted the elbow method[2], a technique used in cluster analysis, to aid determining the optimum number of *HFU* in a given data set.

3.2 The FZI Method

Amaefule *et al* [1993] introduced pore-throat parameters into their definition of *HFU* by rearrangement of the Kozeny-Carman equation (Carman [1961]):

[2] The elbow method is based on the observation that as the number of clusters increases, the sum of within-cluster variance of each cluster is reduced. This is because having more clusters allows to capture finer groups of data objects that are more similar to each other (Han *et al* [2012]).

$$0.0314\sqrt{\frac{k}{\phi}} = \frac{\phi}{1-\phi}\frac{1}{\sqrt{F_s\tau\, S_{gv}}} \tag{3.1}$$

Where F_s is the shape factor, a characteristic parameters of the porous media, τ is the tortuosity, and S_{gv} is the surface area per unit grain volume. The product $F_s\tau^2$ is known as the Kozeny constant, and usually varies between 5 and 100 for most reservoir rocks (Abbaszadeh *et al* [1996]). The constant 0.0314 is the conversion factor from μm^2 to md.

Amaefule *et al* [1993] defined the flow zone indicator (*FZI*), rock quality index (*RQI*) and void ratio (ϕ_z) as in **Equations 3.2** through **3.4**.

$$RQI = 0.0314\sqrt{\frac{k}{\phi}} \tag{3.2}$$

$$\phi_z = \frac{\phi}{1-\phi} \tag{3.3}$$

$$FZI = \frac{1}{\sqrt{F_s\tau\, S_{gv}}} = \frac{RQI}{\phi_z} \tag{3.4}$$

Rearrangement of **Equation 3.1** with definitions in **Equations 3.2** through **3.4** leads to a linear form of the Kozeny-Carman equation after the logarithms are taken on both sides:

$$\log(RQI) = \log(\phi_z) + \log(FZI) \tag{3.5}$$

Equation 3.5 suggests that rocks within a given *HFU* should exhibit a linear trend of unit slope on a log-log plot of *RQI* against ϕ_z. Furthermore, estimation of the *FZI* for each *HFU* can be graphically done by letting ϕ_z be 1. This is because at ϕ_z equal 1 the values of *RQI* and *FZI* are the same. This approach is known as graphical clustering.

In summary, data samples with similar *FZI* values will be close to a single unit-slope straight line with a mean *FZI* value. Conversely, samples with significantly different *FZI* will lie on other parallel unit-slope lines. Each line defines a *HFU* and has associated mean *FZI* value.

Permeability can be predicted for a given *FZI* and porosity values by rearrangement of **Equations 3.2** through **3.4**.

$$k = 1014FZI^2 \frac{\phi^3}{(1-\phi)^2} \tag{3.5}$$

3.3 Hierarchical Cluster Analysis: an Overview

Objective definition of the number of *HFU* and their corresponding FZI values can be achieved through hierarchical Cluster Analysis (Abbaszadeh *et al* [1996] and Dezfoolian *et al* [2013]). This is a method in data mining and statistics in which a hierarchical decomposition of the given data set is done. The method can be classified into agglomerative, if higher order clusters are created, or divisive, if lower order groups are generated to break down starting higher order groups of data objects (Han *et al* [2012]).

Of particular interest in *HFU* characterization is the agglomerative clustering. An agglomerative hierarchical clustering method uses a bottom-up strategy. It typically starts by letting each object form a cluster on its own, and then iteratively merges them into larger (higher order) clusters, until all the objects in the data set are in a single cluster. The result is a tree-like structure called the dendrogram (**Figure 3.1**).

Merging of clusters at each successive step is done in such a way that the similarity between the objects within a given cluster is maximized. At the same time, the dissimilarity with the objects of different clusters is maximized as well. Similarity, and therefore dissimilarity, is based on the

distance between the two objects. Two objects are similar if they are close together. Because two clusters are merged per iteration, where each cluster contains at least one object, an agglomerative method requires at most as many iterations as the number of objects in the data set (Han *et al* [2012]).

Figure 3.1 illustrates the concept of agglomerative hierarchical clustering and the dendrogram. An example data set consisting of 9 objects, A through E, is considered. First, close objects, for example A and B, are merged into one cluster. Then a higher order cluster is formed from objects A, B, J and H. A second cluster is formed containing objects C, D, E, G and F. The resulting dendrogram represents the process of hierarchical clustering in this example.

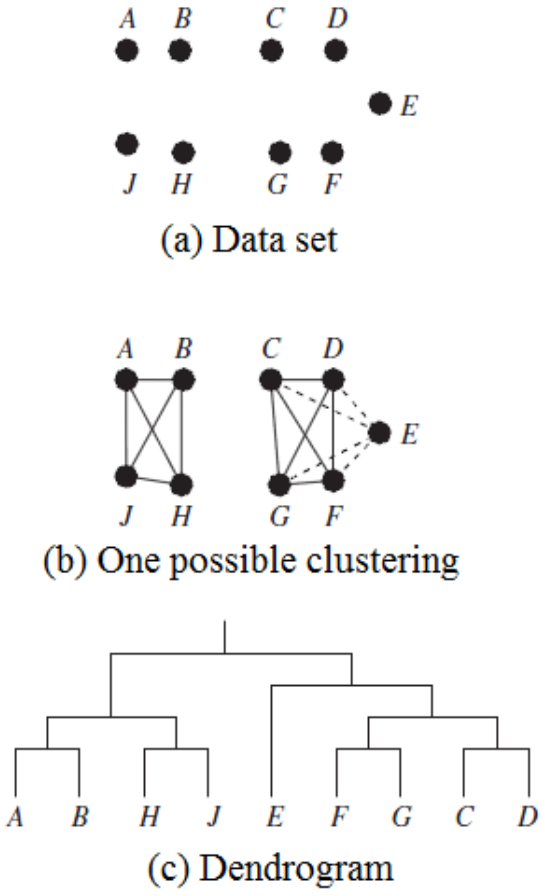

Figure 3.1 Hierarchical clustering and a dendrogram (modified from Han *et al* [2012])

Distance measures used for calculation of similarity, and therefore dissimilarity, between numerical data points include the Euclidean (a.k.a. L_2 norm) and Manhattan (a.k.a. L_1 norm, or City Block) distances. In general, these two are particular cases of a more general measure called the Minkowski distance. The Minkowski distance is also known as the L_p norm. Given two objects x_i and x_j defined in an l-dimensional space, the Minkowski distance is defined by **Equation 3.6**.

$$d(i,j) = \sqrt[p]{\left|x_{i1} - x_{j1}\right|^p + \left|x_{i2} - x_{j2}\right|^p + \cdots + \left|x_{il} - x_{jl}\right|^p} \tag{3.6}$$

Where p is the order. For p=1, then **Equation 3.6** reverts to the Manhattan or City Block measure. For p=2, it reverts to the Euclidean distance.

3.4 Hydraulic Flow Units

More than 800 ft of core data, having about 340 measurements of porosity and permeability were available. An early quality control revealed some plugs were reported damaged by the laboratory, and were dismissed from evaluation. **Figure 3.2** shows valid core porosity and core horizontal permeability data at an average confining stress of 1,330 psi[3]. **Figure 3.2** presents core vertical permeability data. For the purpose of defining hydraulic flow units (*HFU*) however, only the data in **Figure 3.2** is used.

Hierarchical cluster analysis was used instead of the traditional graphical clustering method to objectively determine the number of *HFU* and their associated *FZI* values.

[3] Amaefule *et al* [1993] recommended to use stressed porosity and permeability for evaluation of *HFU*.

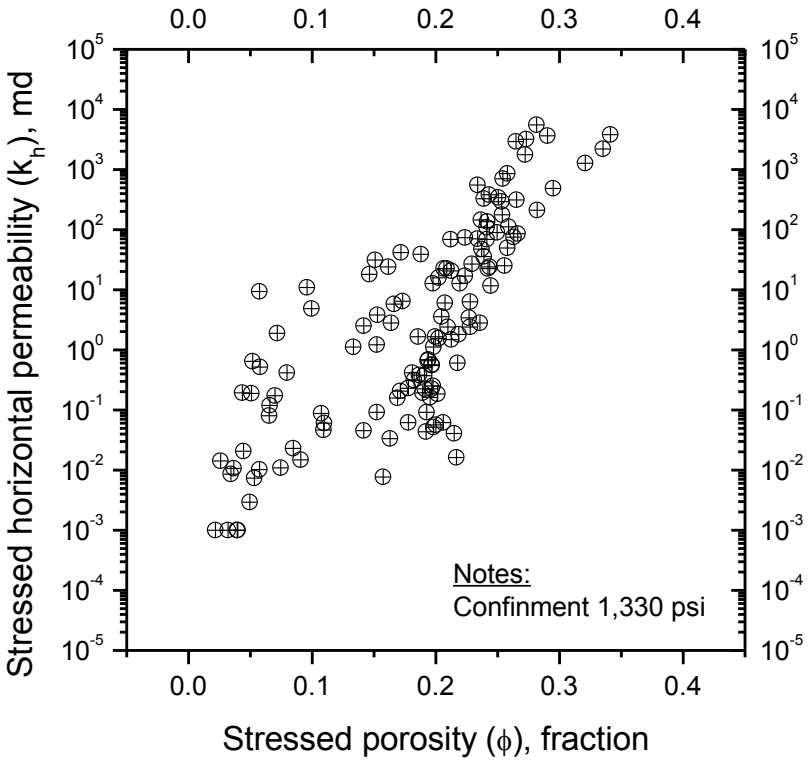

Figure 3.2 Stressed core porosity and core horizontal permeability

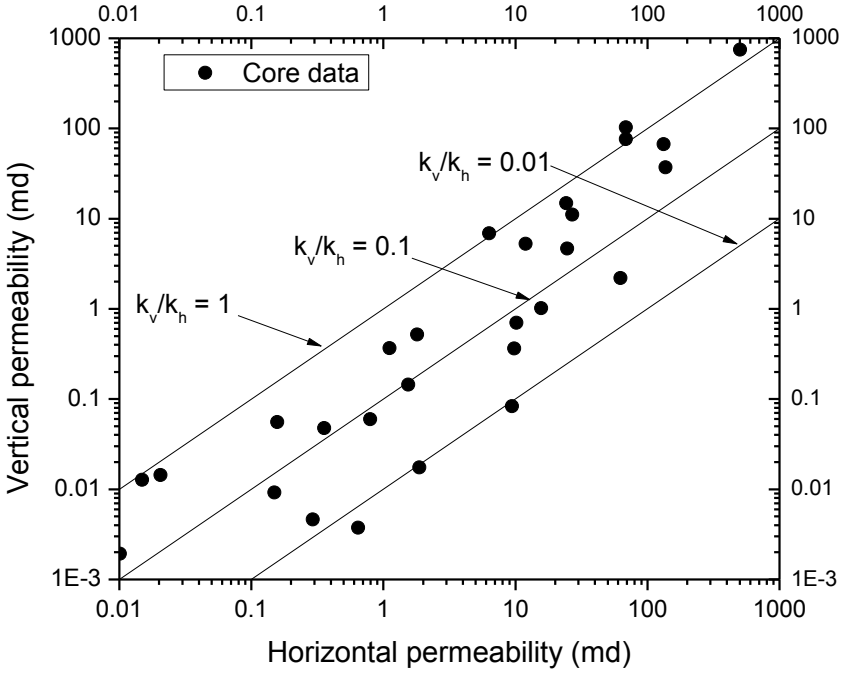

Figure 3.3 Stressed core horizontal and vertical permeability

As discussed earlier, a fundamental need in cluster analysis is to measure the distance between objects. When applied to the identification of *HFU* from core data, an intuitive choice would be to measure distances in a plot of logarithm of *RQI* against logarithm of ϕ_z, as this is the plot used for graphical clustering in the original work by Amaefule *et al* [1993]. Nonetheless, this approach leads to a meaningless clustering as a single straight line in a log-log plot of *RQI* against ϕ_z would intercept more than one cluster or flow unit (**Figure 3.4**).

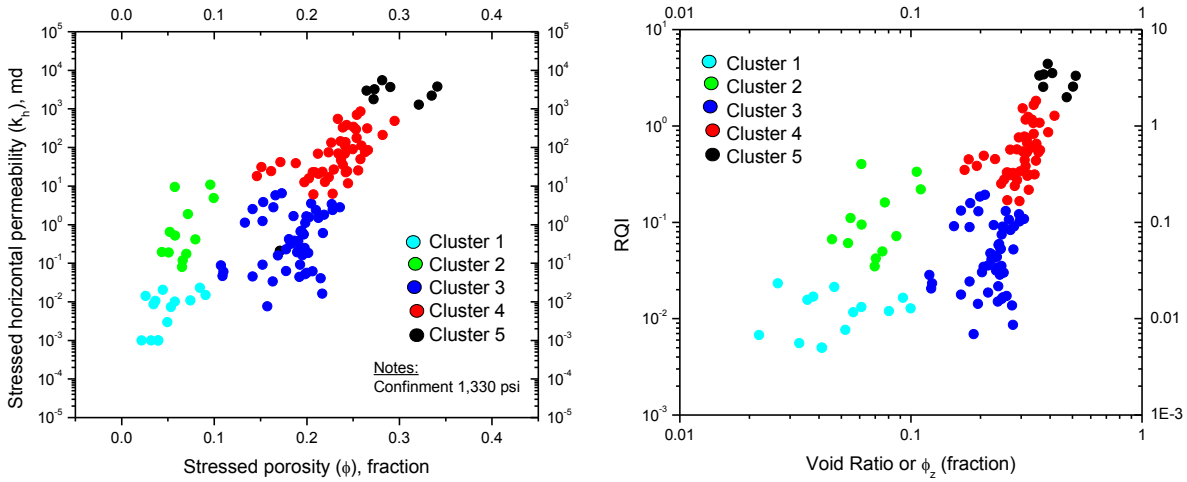

Figure 3.4 Example of an incorrect clustering of *HFU*

Meaningful clusters are obtained when distances are measured on the basis of the logarithm of *FZI* as originally proposed by Abbaszadeh *et al* [1996]. This is because *FZI* values calculated from actual field data usually exhibit a log-normal distribution resulting from the strong dependency of *FZI* on permeability, which is often log-normally distributed.

Hierarchical cluster analysis was implemented in the form of a MATLAB code. The algorithm is presented schematically in **Figure 3.5**. First, stressed core porosity and core permeability data are provided as input. A quality control must be done before to ensure that the input data are reliable. In this case, the laboratory report was inspected and rock samples reported

as damaged were discarded. Next, **Equations 3.2** to **3.4** are used to calculate *FZI* for each data point. Similarity, and thus dissimilarity, measures are obtained on the basis of the logarithm of *FZI* (Abbaszadeh *et al* [1996]). The dendrogram is then built by linkage of the dissimilarity matrix[4].

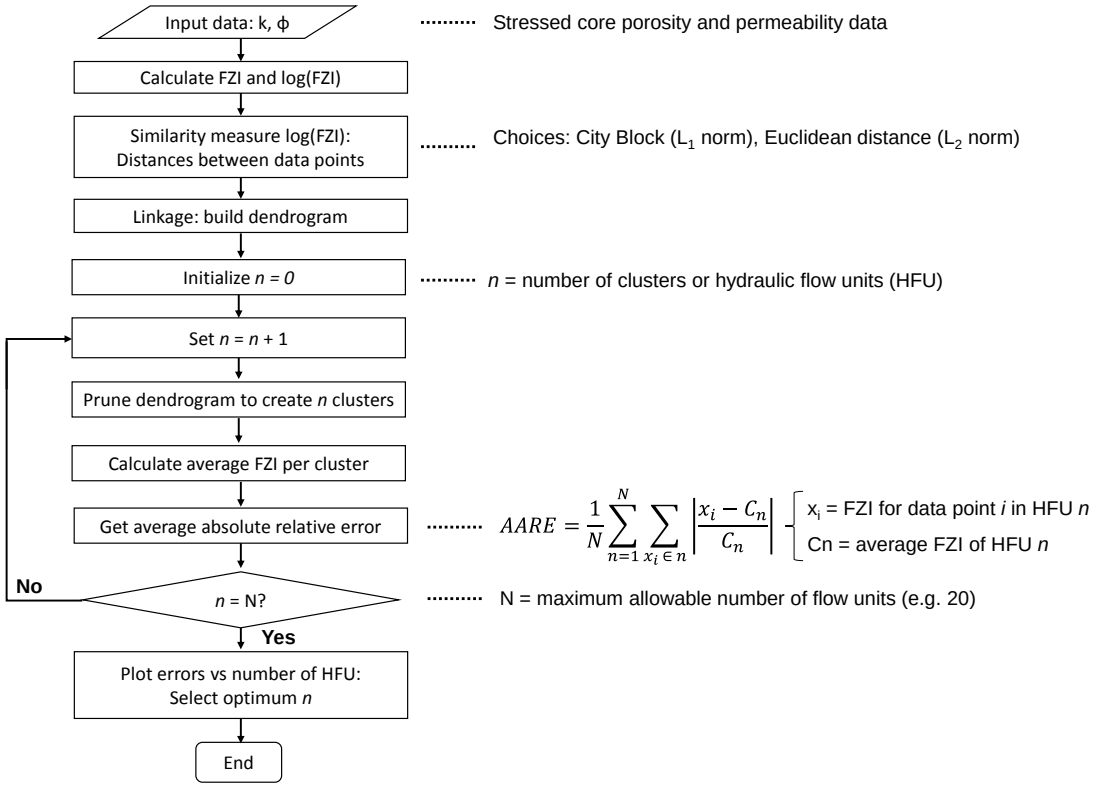

Figure 3.5 Algorithm for hierarchical cluster analysis of hydraulic flow units

Objective definition of the number of *HFU* can be achieved by evaluation of the error in *FZI* for a given number of clusters (Dezfoolian *et al* [2013]). The algorithm in **Figure 3.5** starts by assuming one cluster (i.e. one *HFU*). Then, an average *FZI* is obtained from the data set, and an error metric is evaluated. The number of clusters is then increased, one at a time, up to a

[4] The dissimilarity matrix is a symmetric matrix which stores the collection of distance measures for all pairs of *n* objects, where *n* is the number of data points in the set.

predefined maximum number (*N*). The average *FZI* values per cluster (i.e. per *HFU*) are recalculated and the error metric in *FZI* is reevaluated each time. This process can be thought of as pruning the dendrogram at different levels each time from its base to the top.

Averaging all *FZI* values within given clusters exactly corresponds to a linear least-squares regression of the data (Abbaszadeh *et al* [1996]).

Traditionally, the error metric used in cluster analysis applications is the sum of squared errors, or *SSE* (Han *et al* [2012]). This error metric has also been used for *HFU* characterization by Abbaszadeh *et al* [1996] and Dezfoolian *et al* [2013]. The *SSE* of *FZI* for a given number of N flow units is given by **Equation 3.7**.

$$SSE = \sum_{n=1}^{N} \sum_{x_i \in n} (x_i - C_n)^2 \tag{3.7}$$

Where x_i is the calculated *FZI* value of data point *i* belonging to cluster (i.e. *HFU*) *n*. C_n is the average *FZI* for *HFU n*. And *N* is the maximum number of clusters. In **Equation 3.7**, the inner summation is the within-cluster sum of squared deviations. The outer summation is the sum of all cluster's deviations.

Another error metric is the average absolute relative error in *FZI*. This is defined in **Equation 3.8**.

$$AARE = \frac{1}{N} \sum_{n=1}^{N} \sum_{x_i \in n} \left| \frac{x_i - C_n}{C_n} \right| \tag{3.8}$$

Variables in **Equation 3.8** have the same definition as in **Equation 3.7**.

Regardless of the error metric used, as the number of clusters, i.e. *HFU*, increases, the error metric decreases. This is because the data set is being fit with an increasing number of functional relationships (i.e. unit-slope straight lines in a plot of logarithm of *RQI* against logarithm of ϕ_z).

Once the algorithm in **Figure 3.5** has evaluated the associated error metric for a predefined maximum number of *HFU*, which in this case was 20, the error metric is plotted against the number of clusters. **Figure 3.6** shows this plot, where the error metric is the *AARE*. The same shape is obtained if *SSE* is plotted instead.

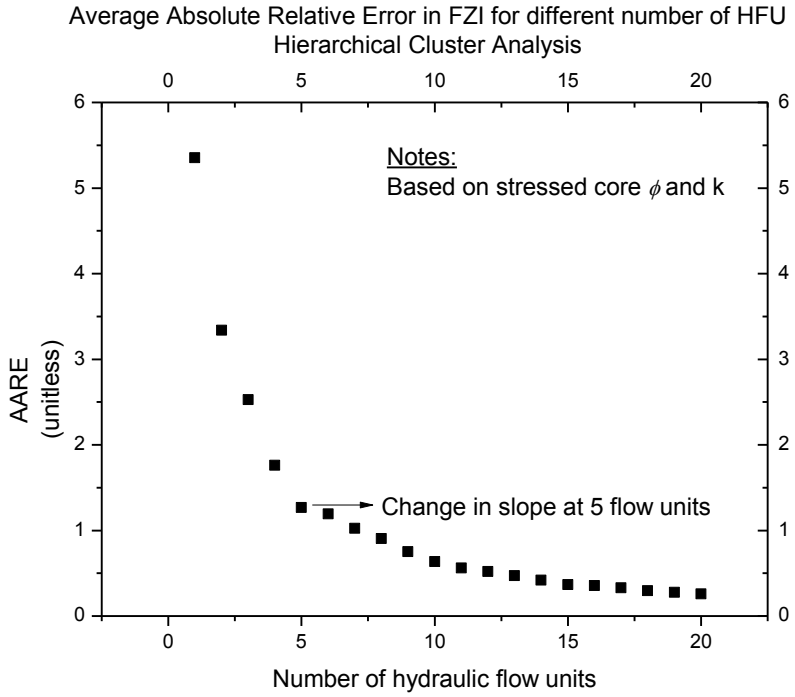

Figure 3.6 Average absolute relative error (*AARE*) in *FZI* from hierarchical cluster analysis of hydraulic flow units (*HFU*). Estimation of the optimum number of *HFU*

In **Figure 3.6**, a visible change in the curvature of the plot is observed. This point represents the optimum number of clusters, i.e. *HFU*, in the data set. This approach is known as the elbow method in cluster analysis (Han *et al* [2012]). At that point, a low error metric in *FZI* is

attained with a small number of clusters, or *HFU*. For the core data set considered (**Figure 3.2**), the optimum number of *HFU* is 5.

Figure 3.7 shows the log-log plot of *RQI* against ϕ_z for the core data in **Figure 3.2**. The average *FZI* values obtained for the five *HFU* define the straight lines drawn in the plot. All data points are associated an *HFU* based on the proximity with each straight line. Rock samples associated to the green *HFU*, called *HFU 5*, exhibit the highest reservoir rock quality, whereas the blue *HFU*, called *HFU 1*, would act as a flow baffle or flow barrier. In **Figure 3.7**, data points labeled as outliers can be grouped into a sixth flow unit by the cluster analysis algorithm. However, since their associated *FZI* value (0.0432) is extremely low, they are considered non-reservoir rock and therefore were excluded from subsequent analysis.

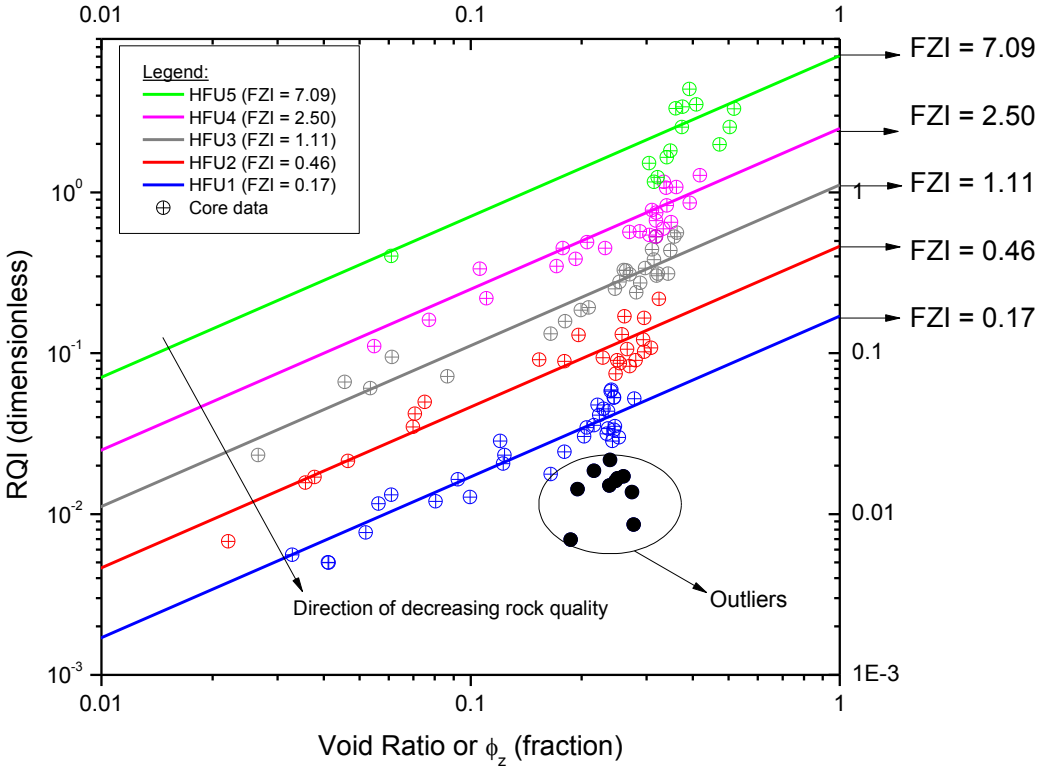

Figure 3.7 Log-log plot of *RQI* vs ϕ_z showing the identified *HFU* from hierarchical cluster analysis

Table 3.1 summarizes the average *FZI* values found for each hydraulic flow unit.

Table 3.1 Average *FZI* values for each *HFU*

HFU	**Average FZI** (unitless)
1	0.17
2	0.46
3	1.11
4	2.50
5	7.09

Equation 3.5 was used next to obtain permeability given *FZI* in **Table 3.1** for a wide range of porosity values. The resulting permeability is plotted as colored curves in **Figure 3.8**. Measured core data is also included in this plot for comparison with the derived permeability for each *HFU*.

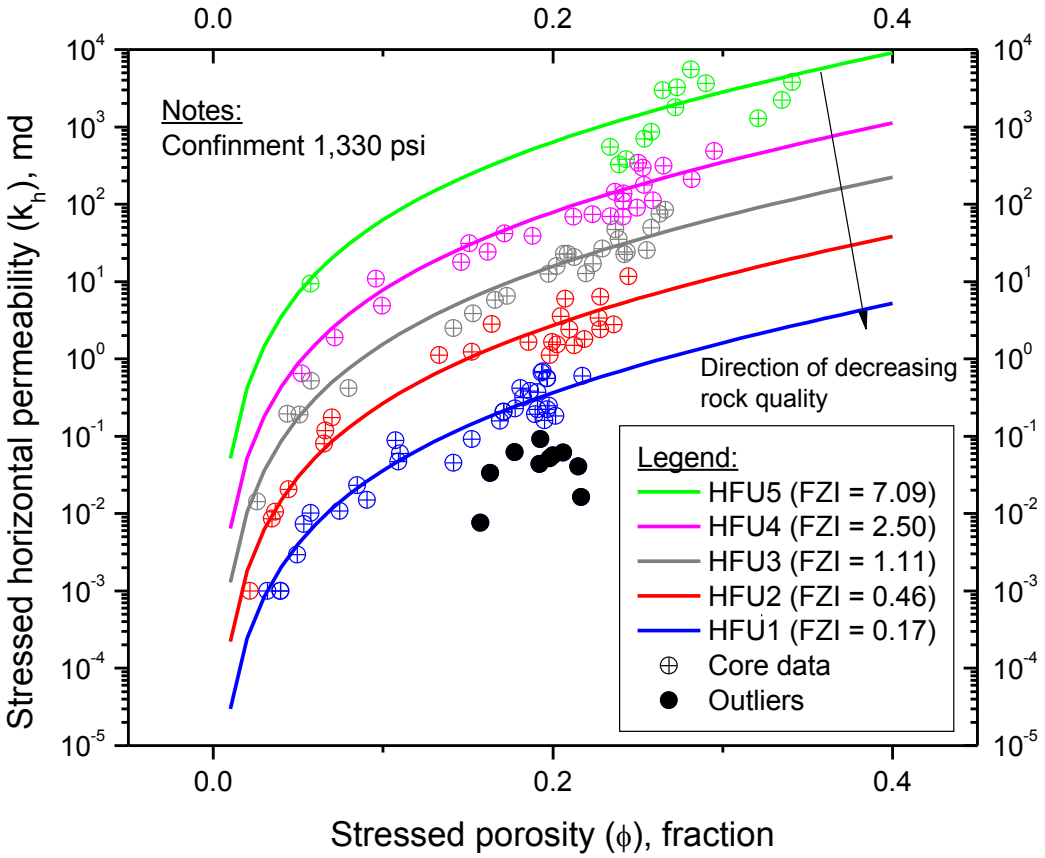

Figure 3.8 Stressed core data and permeability derived from FZI values for each HFU

3.5 Rock-Fluid Properties

Rock-fluid properties, such as relative permeability and capillary pressure, were assigned to each *HFU*. This was done primarily because these properties are required as input for numerical simulation. In addition, this can also be viewed as a consistency check. Since by definition each *HFU* groups rocks having similar parameters that influence fluid flow, it is to be expected that distinct characteristics exist between relative permeability and capillary pressure for each *HFU*. Morgan and Gordon [1970] discussed this and presented some examples. They, however, used the notion of *rock type*, instead of *HFU*. For all practical purposes these two concepts can be used interchangeably as in Tiab and Donaldson [2016].

Ten primary imbibition water-oil relative permeability tests, ten primary drainage gas-oil relative permeability tests and eight primary drainage porous plate capillary pressure tests were available. A quality control revealed two relative permeability tests were unreliable and were dismissed for analysis.

3.5.1 Primary imbibition water-oil relative permeability data

All available tests were run using the unsteady state method. The process involved displacement of oil by water (i.e. primary imbibition of a water-wet rock). **Table 3.2** and **Figures 3.9** through **3.19** summarize the experimental data, which was assigned a *HFU* based on their *FZI* values. As noted by Morgan and Gordon [1970] and other authors, there is a relationships between rock properties, pore geometry, and relative permeability. Note from **Table 3.2** that as *FZI* increases, the different measured parameters exhibit a specific, and consistent, trend. For instance, the irreducible water saturation (S_{wir}) decreases. This is because rocks with large pores have smaller surface area (Morgan and Gordon [1970]). Furthermore, the endpoint oil relative

permeability, that is k_{ro} at S_{wir}, also increases, while remains larger than the endpoint water relative permeability (k_{rw} at S_{orw}), which also increases as *FZI* increases. In fact, Morgan and Gordon [1970] noted that curves with high end points and low irreducible water saturations, are characteristic of reservoir rocks with large open pores.

Moreover, final k_{rw} values are lower than initial k_{ro} values in water-wet rocks, because the residual oil occupies a portion of the largest pores. Also note from **Table 3.2** that the mobile oil saturation also increases as the rock quality, or *FZI*, increases. This means that two-phase flow occurs over a broader range of saturation for higher quality rocks.

An observation from **Figures 3.11** and **3.13** is that, within a given *HFU*, water-oil relative permeability characteristics are very similar, varying only for rather large changes in absolute permeability.

Table 3.3 shows the experimental microscopic displacement efficiencies at residual oil saturation (E_{Dmax}) for each test. E_{Dmax} was estimated from **Equation 3.9** (Satter *et al* [2008]).

$$E_{Dmax} = \frac{1-S_{wir}-S_{orw}}{1-S_{wir}} = 1 - \frac{S_{orw}}{S_{oi}} \tag{3.9}$$

Where S_{orw} is the residual oil saturation after waterflood, and S_{oi} is the initial oil saturation. Values of E_{Dmax} in **Table 3.3** reveal, as expected, that waterflood is potentially more effective in high quality rocks such as *HFU 4* and *HFU 5*.

Table 3.2 Unsteady state water-oil relative permeability tests

Parameter	Test #1	Test #2	Test #3	Test #4	Test #5	Test #6	Test #7	Test #8
HFU	1	2	3	3	4	5	5	5
k, md	0.602	1.49	25.63	84.90	379.89	860.10	1782.7	3651.0
ϕ , fraction	0.217	0.213	0.256	0.276	0.243	0.258	0.272	0.290
FZI	0.188	0.308	0.916	1.443	3.861	5.215	6.793	8.614
S_{wir}, fraction	0.675	0.650	0.528	0.521	0.530	0.431	0.370	0.304
S_{orw}, fraction	0.142	0.132	0.142	0.149	0.121	0.138	0.149	0.198
k_{ro} at S_{wir}, fraction	0.121	0.174	0.518	0.472	0.562	0.838	0.873	0.815
k_{rw} at S_{orw}, fraction	0.004	0.005	0.047	0.031	0.035	0.087	0.138	0.143
Mobile S_o, fraction	0.182	0.218	0.330	0.330	0.349	0.431	0.480	0.498

Table 3.3 Displacement efficiency at residual oil saturation after waterflood from unsteady state water-oil relative permeability tests

Parameter	Test #1	Test #2	Test #3	Test #4	Test #5	Test #6	Test #7	Test #8
HFU	1	2	3	3	4	5	5	5
E_{Dmax}	56.1%	62.4%	69.9%	68.9%	74.3%	75.7%	76.3%	71.6%

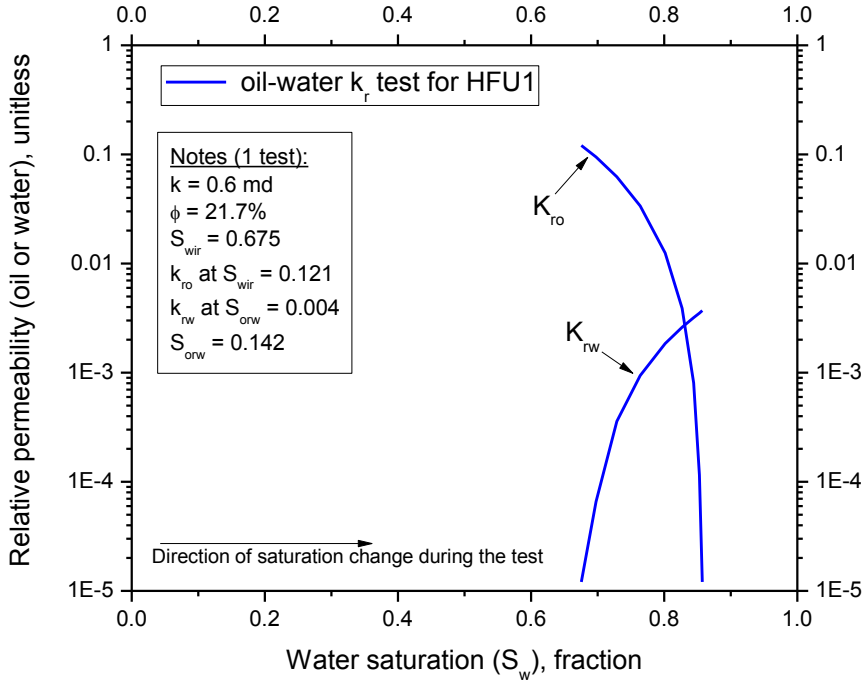

Figure 3.9 Water-oil unsteady state relative permeability test done on a core plug sample belonging to *HFU* 1

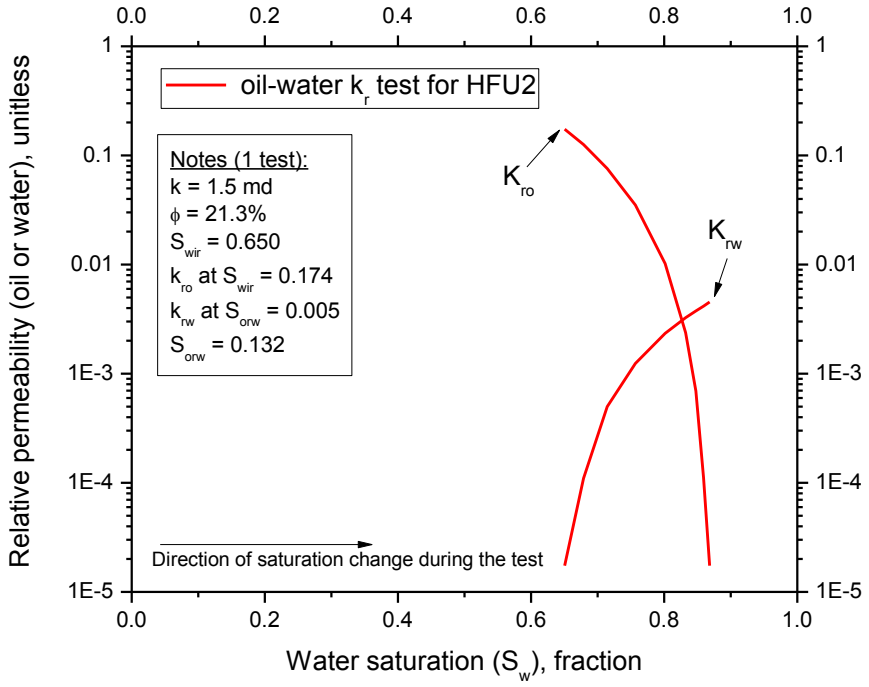

Figure 3.10 Water-oil unsteady state relative permeability test done on a core plug sample belonging to *HFU* 2

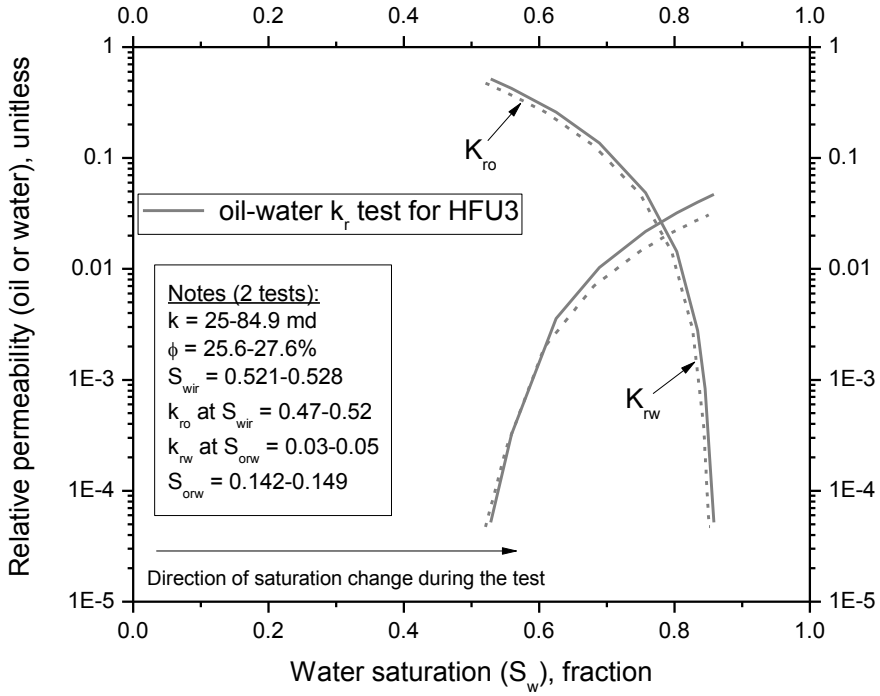

Figure 3.11 Water-oil unsteady state relative permeability tests done on a core plug sample belonging to *HFU* 3

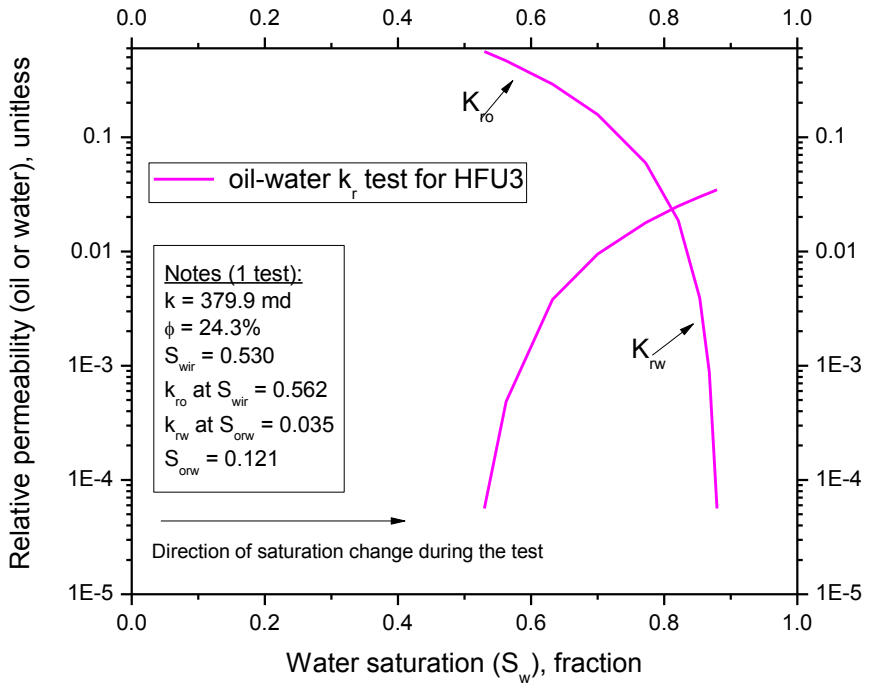

Figure 3.12 Water-oil unsteady state relative permeability test done on a core plug sample belonging to HFU 4

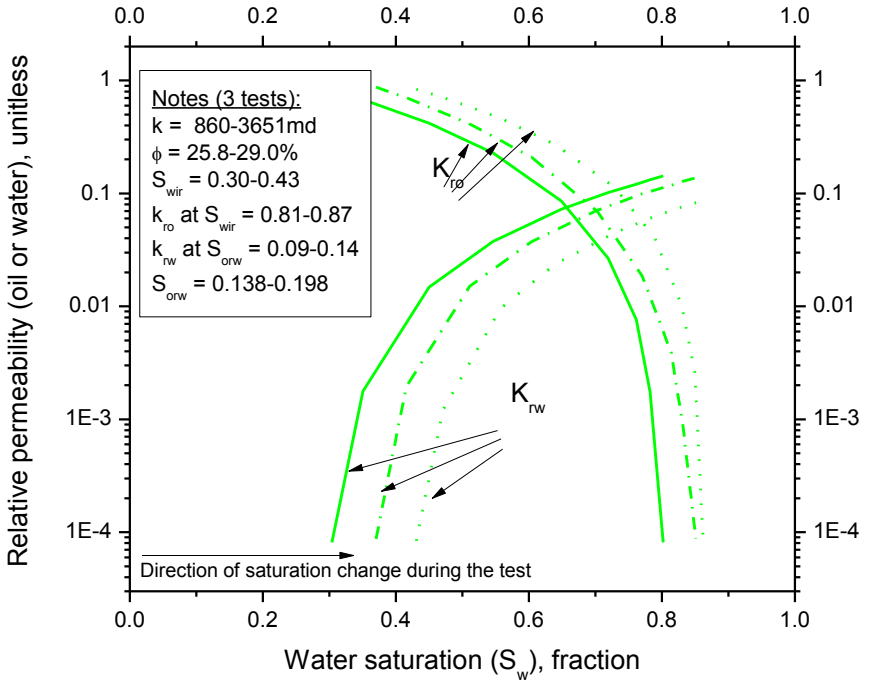

Figure 3.13 Water-oil unsteady state relative permeability tests done on a core plug sample belonging to *HFU* 5

Finally, despite the evident differences in *FZI* among the tested samples, the amount of oil remaining after waterflood (i.e. S_{orw}) is relatively invariant among all five *HFU*. This can be seen in **Table 3.2** and **Figure 3.14**. **Figure 3.14** is the initial-residual saturation plot. Land [1967] and Land [1971] showed that the residual, or trapped, saturation of a non-wetting phase is function of its initial saturation and a parameter, called Land's trapping constant (*C*). Land's model is the most widely used trapping model (Spiteri *et al* [2008]). Values of *C* for various formations have been reported in the literature, with values generally lower than 5 (Blunt [2017] and van Golf-Racht [1982]). The best estimation for a given rock however, is obtained through data fitting of experimental data (van Golf-Racht [1982]). In **Figure 3.14**, experimental data was fitted with *C* equal 4.5. This relationship serves as an input for numerical simulation of waterflood processes. From given values of S_{oi} per gridblock, S_{orw} is defined for all cells in the model given a known *C*.

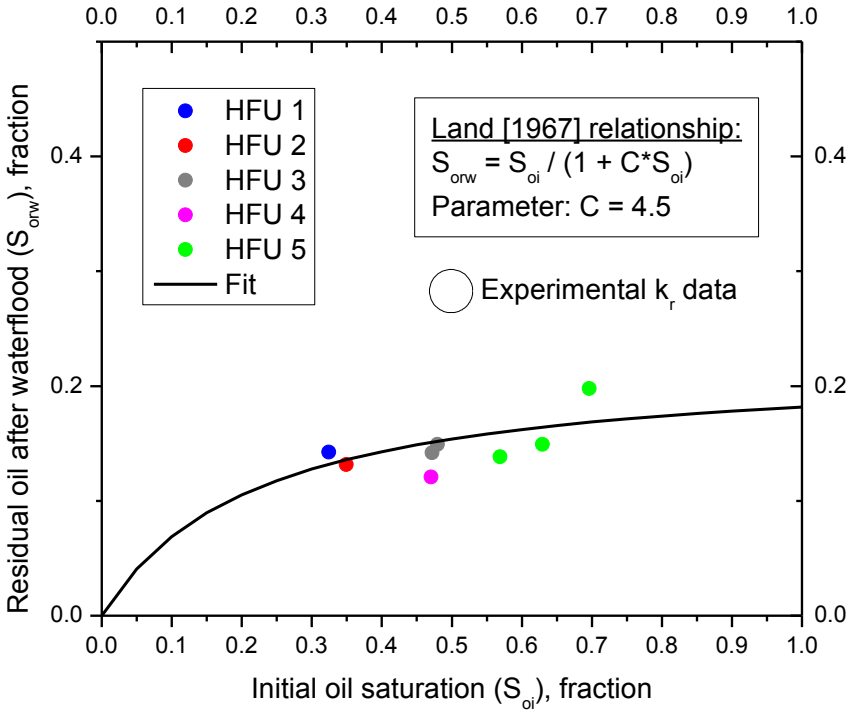

Figure 3.14 Experimental initial-residual saturation plot for immiscible displacement of oil by water

3.5.2 Primary drainage gas-oil relative permeability data

As in the case of the water-oil system, all gas-oil relative permeability tests were run using the unsteady state method. Core plugs were the same for both tests, but the process in this case involves primary drainage (i.e. gas displacing oil). **Table 3.4** and **Figures 3.15** through **3.19** summarize the experimental data. Note that k_{ro} at S_{wir} is the same in oil-water and gas-oil systems (**Tables 3.2** and **3.4**), as this is a consistency requirement. Additionally, the final (i.e. endpoint) gas relative permeability (k_{rg} at S_{org}) is larger than k_{rw} at S_{orw} in **Table 3.2**. This is because gas is the least wetting phase, and thus, tends to occupy the larger pores. The later remark is also evident graphically from **Figures 3.15** through **3.19** by inspection of the intersection point of the curves. The gas saturation at which oil and gas relative permeabilities are equal is heavily displaced toward lower gas saturation values. Also, values for E_{Dmax} in **Tables 3.3** and **3.5** are remarkably similar.

Table 3.4 Unsteady state gas-oil relative permeability tests

Parameter	Test #1	Test #2	Test #3	Test #4	Test #5	Test #6	Test #7	Test #8
HFU	1	2	3	3	4	5	5	5
k, md	0.602	1.49	25.63	84.90	379.89	860.10	1782.7	3651.0
ϕ , fraction	0.217	0.213	0.256	0.276	0.243	0.258	0.272	0.290
FZI	0.188	0.308	0.916	1.443	3.861	5.215	6.793	8.614
S_{wir}, fraction	0.675	0.650	0.528	0.521	0.530	0.431	0.370	0.304
S_{org}, fraction	0.147	0.142	0.152	0.155	0.135	0.149	0.155	0.201
k_{ro} at S_{wir}, fraction	0.121	0.174	0.518	0.472	0.562	0.838	0.873	0.815
k_{rg} at S_{org}, fraction	0.17	0.030	0.188	0.163	0.211	0.252	0.417	0.356
Mobile S_o, fraction	0.182	0.218	0.330	0.330	0.349	0.431	0.480	0.498

Table 3.5 Displacement efficiency at residual oil saturation after gas flood from unsteady state gas-oil relative permeability tests

Parameter	Test #1	Test #2	Test #3	Test #4	Test #5	Test #6	Test #7	Test #8
HFU	1	2	3	3	4	5	5	5
E_{Dmax}	54.8%	59.5%	67.8%	67.7%	71.3%	73.9%	75.3%	71.1%

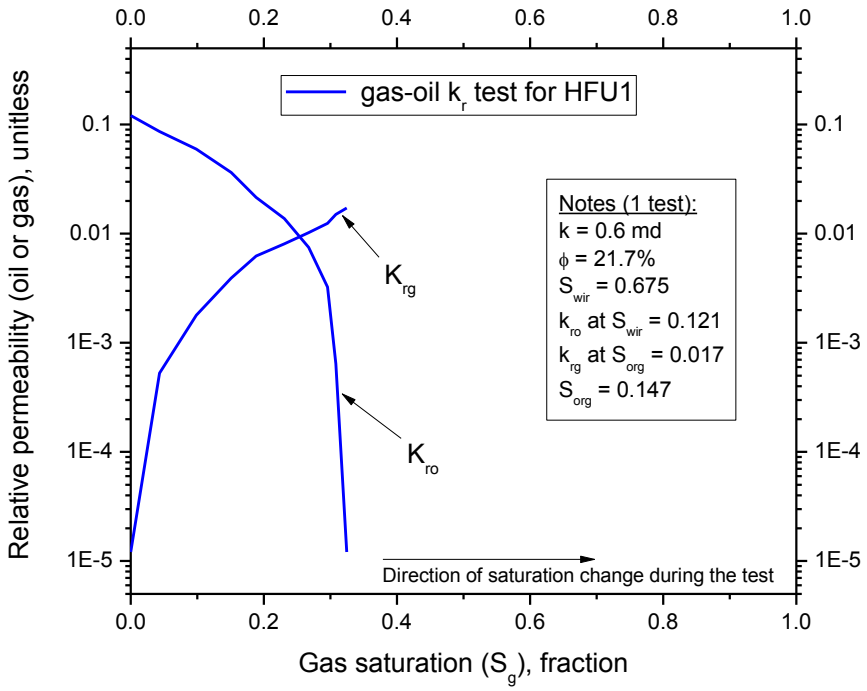

Figure 3.15 Gas-oil unsteady state relative permeability test done on a core plug sample belonging to *HFU1*

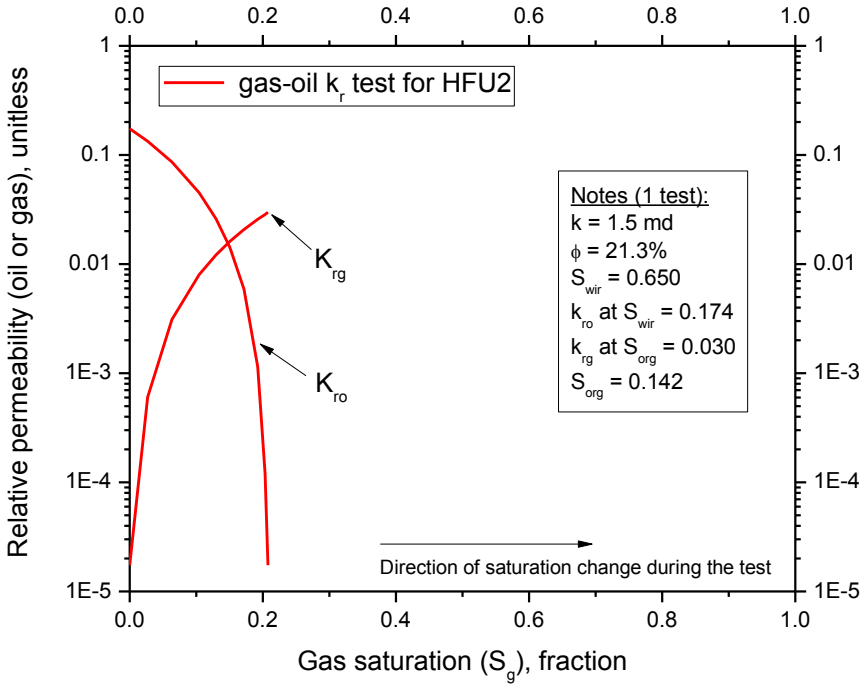

Figure 3.16 Gas-oil unsteady state relative permeability test done on a core plug sample belonging to *HFU2*

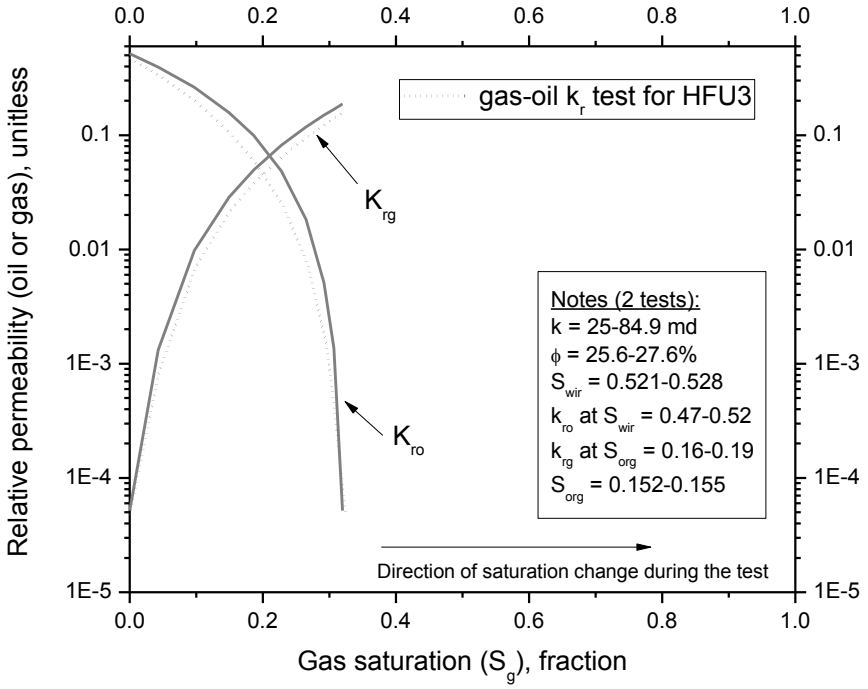

Figure 3.17 Gas-oil unsteady state relative permeability tests done on a core plug sample belonging to *HFU3*

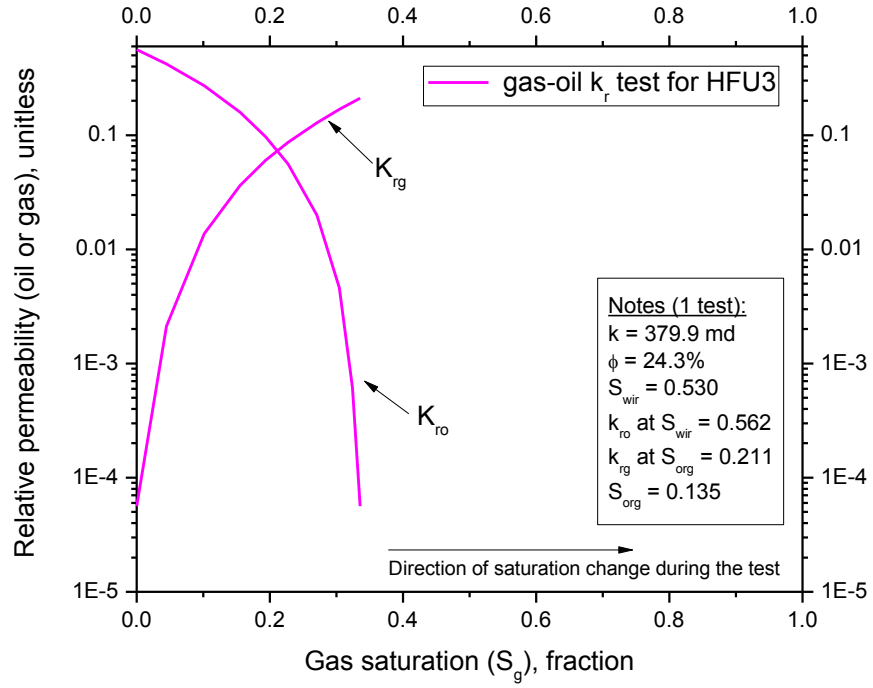

Figure 3.18 Gas-oil unsteady state relative permeability test done on a core plug sample belonging to *HFU4*

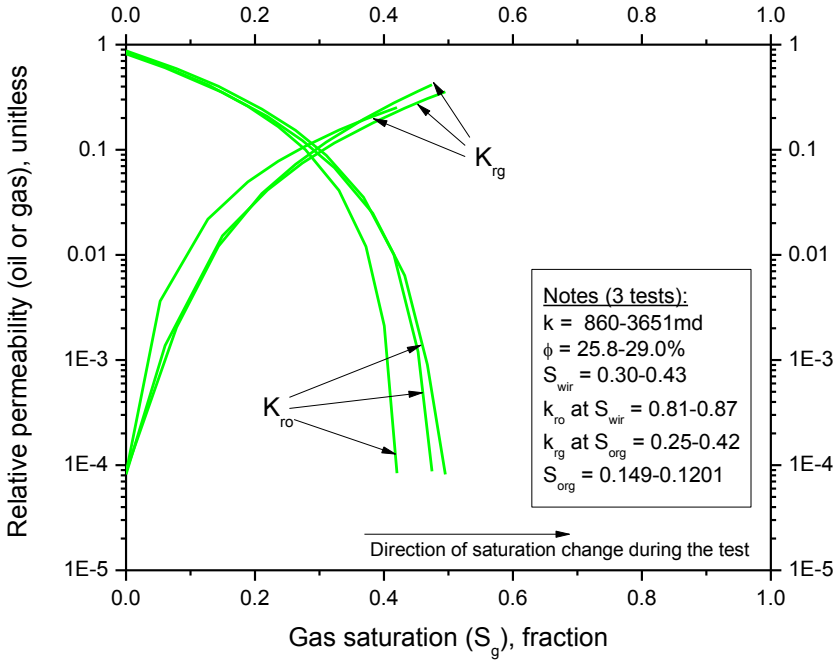

Figure 3.19 Gas-oil unsteady state relative permeability tests done on a core plug sample belonging to *HFU5*

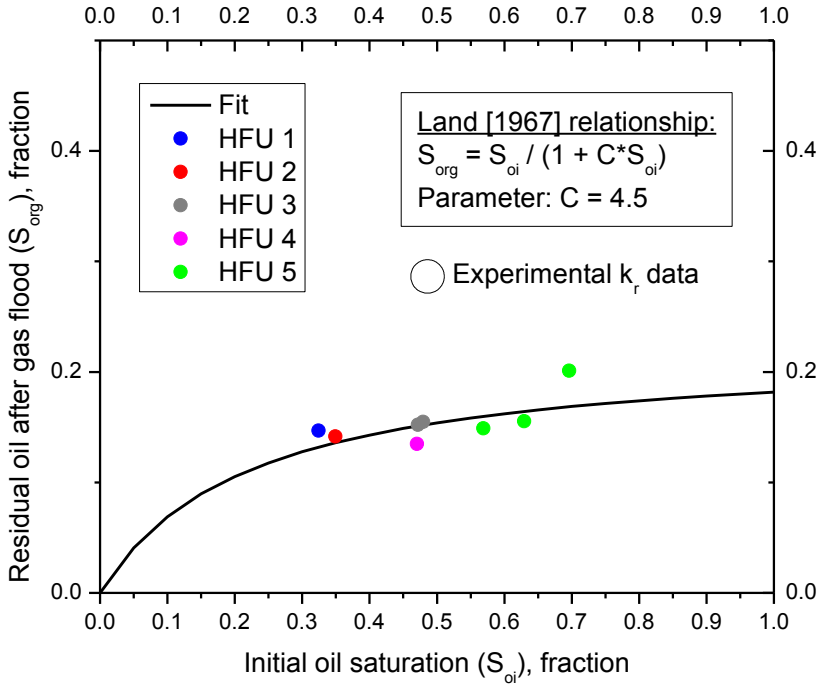

Figure 3.20 Experimental initial-residual saturation plot for immiscible displacement of oil by gas

Figure 3.20 shows the initial-residual saturation plot for the immiscible displacement of oil by gas. Notably, the residual oil saturation after gas flood (S_{org}) is similar to S_{orw} (**Figure 3.14**)[5]. For this reason, a trapping constant (C) of 4.5 is also used to fit the data.

3.5.3 Primary drainage oil-water capillary pressure data

Capillary pressure tests were conducted using the porous plate method. Laboratory data was converted to reservoir conditions (Dandekar [2013]) to account for the pertinent interfacial tension and contact angle. **Table 3.6** and **Figure 3.21** summarize the experimental data. Consistency with the *HFU* characterization is observed. For example, in **Figure 3.21**, *FZI* increases from right to left. Low quality *HFU* take their place to right in the plot, as S_{wir} is larger. High quality rock samples, belonging to *HFU 5*, also display a flatter shape toward low capillary pressure values, suggesting their pore size distribution is relatively homogeneous. Conversely, lower quality rocks, such as *HFU 2*, display a non-flat capillary pressure curve, indicating higher heterogeneity and lower grain sorting (Archer and Wall [1986]). **Figure 3.22** shows the relationship between S_{wir} and rock permeability from all experiments (relative permeability and capillary pressure). As rock permeability (and thus *FZI*) increases, S_{wir} consistently decreases.

Table 3.6 Oil-water capillary pressure tests

Parameter	Test #1	Test #2	Test #3	Test #4	Test #5	Test #6	Test #7	Test #8
HFU	2	2	3	3	4	5	5	5
k, md	3.560	4.320	58.400	83.900	596.00	2549.0	3050.0	4931.0
ϕ , fraction	0.237	0.229	0.260	0.265	0.303	0.334	0.342	0.351
FZI	0.391	0.461	1.337	1.549	3.197	5.461	5.761	6.882
S_{wir}, fraction	0.696	0.612	0.558	0.497	0.409	0.354	0.324	0.315

[5] This is, most likely, because the capillary numbers (N_{vc}) involved in the displacement of oil by water and the displacement of oil by gas did not differ enough to cause a significant change in desaturation of oil from the samples. N_{vc} is a dimensionless ratio of viscous to local capillary forces (Lake *et al* [2014]).

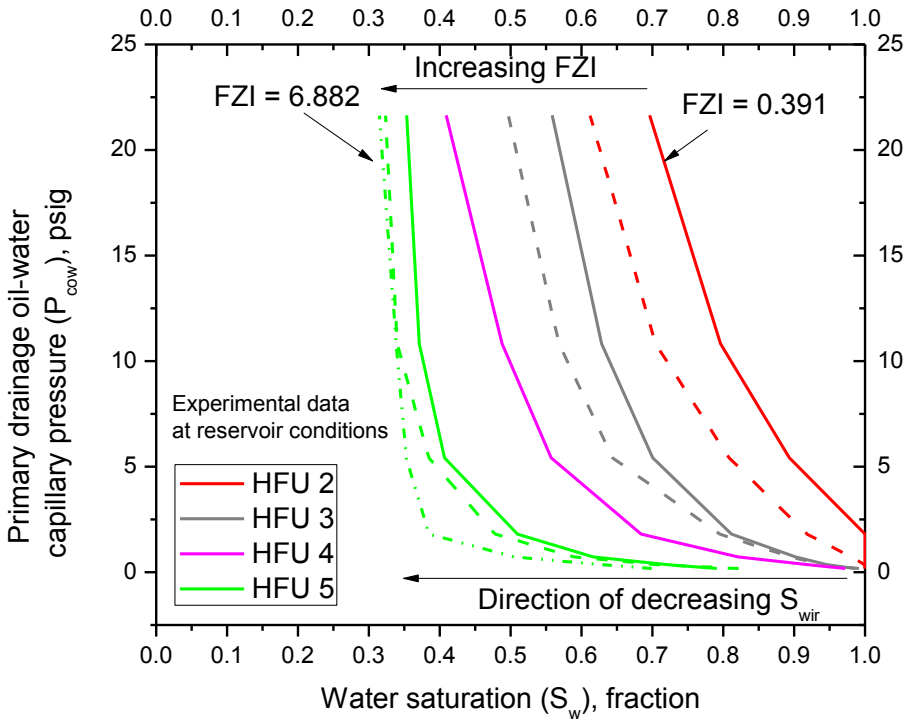

Figure 3.21 Oil-water capillary pressure tests at reservoir conditions

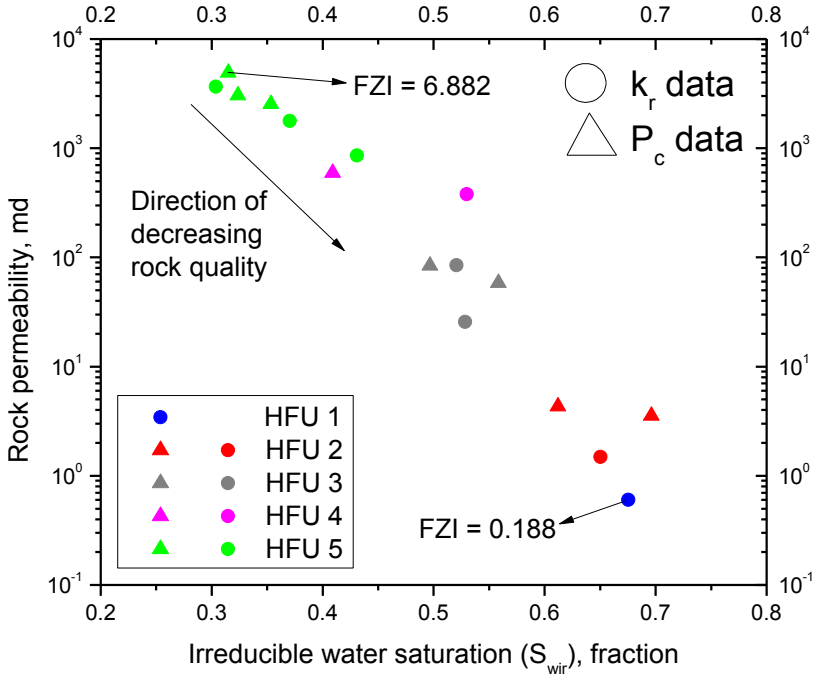

Figure 3.22 Relationship between experimental irreducible water saturation and rock permeability

3.6 General Sedimentological Features

Fluid flow through porous media is significantly controlled by pore-throat geometrical attributes (Abbaszadeh *et al* [1996]). These in turn respond to mineralogy (e.g. clay content and distribution[6], matrix and cement abundance, etc.) and texture (grain size and shape, sorting, packing, etc.). Various combinations of these properties can lead to distinct geological facies (i.e. lithofacies) that have similar fluid transport characteristics. Therefore, *HFU* not often exactly correspond to lithofacies. Moreover, *HFU* are seldom vertically continuous, thus boundaries of *HFU* and lithofacies may differ (Cannon [2018]).

Following the work by Amaefule *et al* [1993], however, a link between *HFU* and lithofacies was attempted. The merit in doing this is to help guide the distribution of *HFU* in 3D space based on a prior facies model.

Based on an available sedimentological report[7] covering about 100 ft of rock samples distributed over 600 ft along the cored column of the producing formation, the likely depositional environment has been described as a fluvially-dominated delta. Dikkers [1985] pointed out that deltaic formations are a favorite habitat for hydrocarbon accumulations.

Figures 3.23 and **3.24** show thin sections and photos at different depths in the core. The pore size increases as the rock quality, which is characterized by an *FZI* value, increases (**Figure 3.23**). Remarkably, *HFU 5* has the largest pore-throat aperture in thin sections. This explains why the relative permeability curves (**Figures 3.13** and **3.19**) display high end point values, low irreducible water saturations (S_{wir}), and a broader range of saturations over which two phase flow

[6] Types of clay distribution include structural, laminar and disperse (Schön [2011]).
[7] Source is held confidential.

occurs. Conversely, *HFU1* has the smallest pore throats, and this causes the relative permeability curves to have the lowest end point values and highest S_{wir} (**Figures 3.9** and **3.15**). In general, pore sizes and pore-throat aperture monotonically increase from *HFU1* through *HFU5* while S_{wir} monotonically decreases. This can be observed by naked eye from the color of the rock samples shown in **Figure 3.24**, and also explains the relationship shown in **Figure 3.22**.

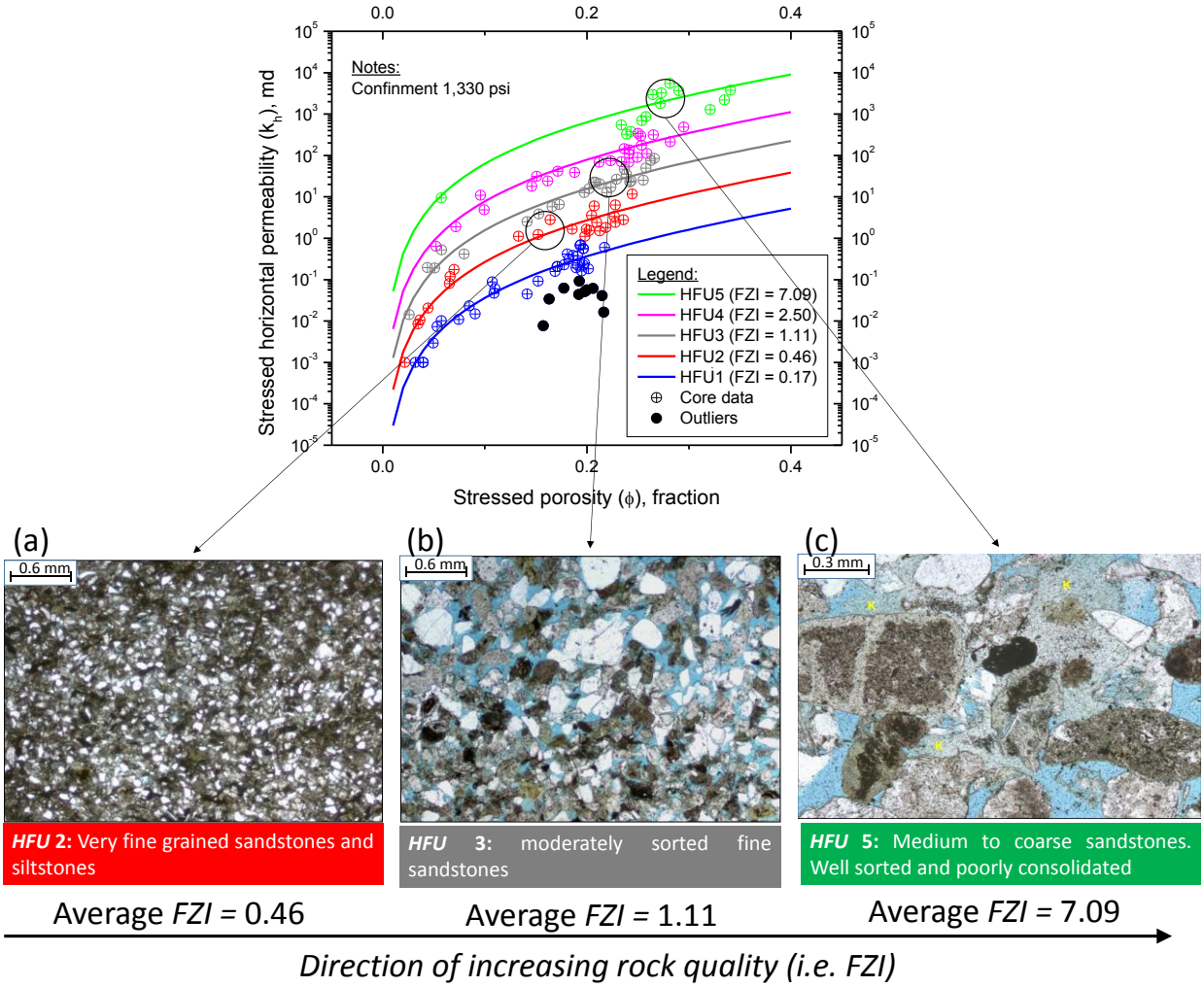

Figure 3.23 Thin sections for three of the five hydraulic from units: *HFU2* (a), *HFU3* (b) and *HFU5* (c) (figures a, b and c printed with permission from Zeus OL Peru SAC [2016])

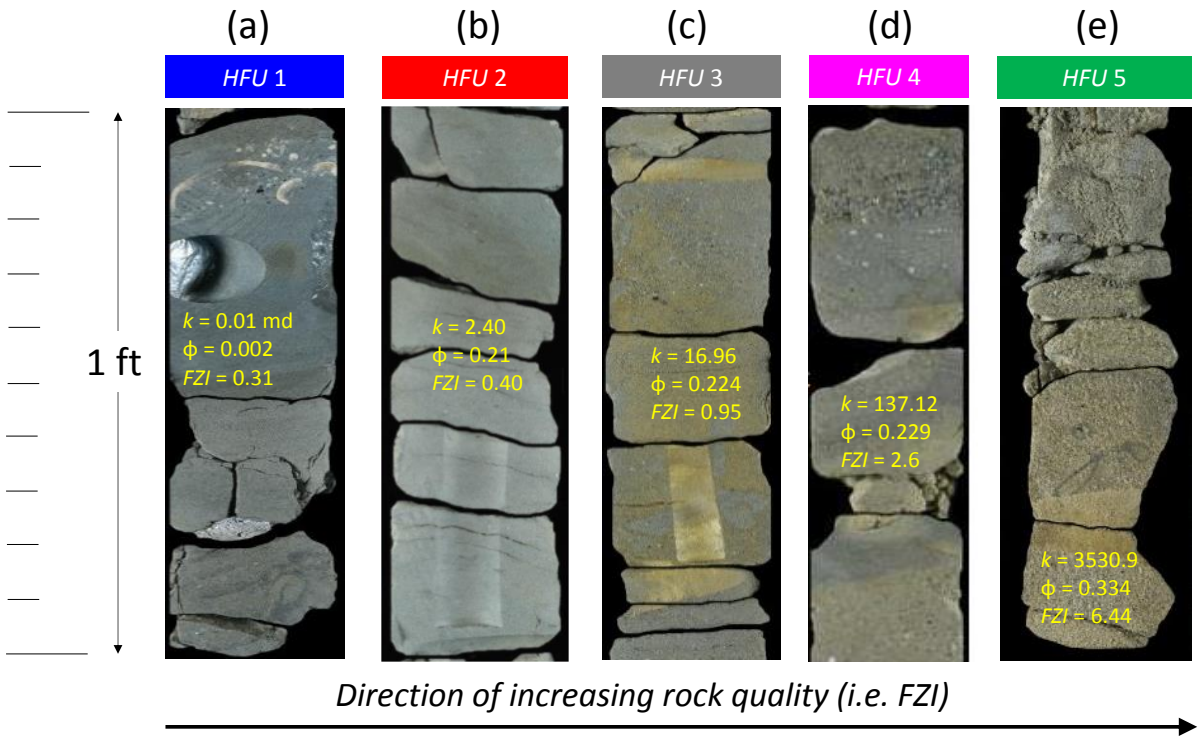

Figure 3.24 Core photos showing variations in rock texture (figures a through e printed with permission from Zeus OL Peru SAC [2016])

Hydraulic flow unit *HFU1* corresponds, in general, to intercalated claystones and siltstones. Rocks exhibit finely laminated to massive sedimentary structures (**Figure 3.24a**). Deposition likely occurred in a low-energy environment, described as a subaqueous interlobe area. For all practical purposes, these rocks act as a flow baffle or flow barrier.

Rocks characterized as *HFU2*, on the other hand, have been described as very fine grained sandstones, silty sandstones and sandy siltstones. They generally exhibit massive (**Figure 3.24b**) or laminated sedimentary structures with moderate bioturbation.

HFU3 tends to comprise moderately sorted, fine and coarse sandstones (**Figure 3.24c**). Rocks have been described as locally calcareous, having clayey cement and presence of clasts, as a result of episodic changes in fluvial sediment supply.

Rocks within *HFU4* include very well sorted sandstones and locally calcareous sandstones having, in general, massive sedimentary structures (**Figure 3.24d**). This flow unit also includes conglomerates, having volcanic clasts and bioclasts[8], likely transported by strong fluvial currents.

Finally, rocks characterized as *HFU5* have been described as medium to coarse and very coarse grained sandstones. They are well sorted and generally poorly consolidated. Bioturbation is scarce but not absent. These characteristics are suggestive of a high-energy landward environment.

3.7 Summary

From available core data, which covers more than 800 ft of rock, five hydraulic flow units (named *HFU1* through *HFU5*) were identified. This analysis was done in an objective manner by use of hierarchical cluster analysis. The implementation was done in the form of a MATLAB code. The algorithm automatically determined the optimum number of flow units and their associated *FZI* values. Distinct permeability-porosity relationships were defined for each flow unit. These relationships allow to estimate permeability in uncored, but logged wells, given known values of *FZI* and porosity.

The resulting flow units were also associated rock-fluid properties, such as relative permeability and capillary pressure, obtained from experimental analysis. Consistency was observed, for example, it was noted that as rock quality increases from *HFU1* to *HFU5*, S_{wir} monotonically decreases and relative permeability end points monotonically increase. Finally, major sedimentological features were recognized for each flow unit.

[8] Sediments from organic materials (e.g. bivalve fragments).

CHAPTER IV

SUMMARY AND RECOMMENDATIONS

4.1 Summary

In this study, a reservoir fluid and rock characterization was done for a Peruvian oil reservoir. The following are major summarizing remarks:

a. Lack of *PVT* data from actual fluid samples was overcome by integrating analog *PVT* studies, production and pressure data, well logs, and reliable fluid property correlations, such as those in McCain *et al* [2011].
b. Analog fluid samples were validated by comparison of experimental and theoretical equilibrium ratios, or *k*-factors. Fluid samples were deemed as valid since the sampled gas and liquid were in equilibrium at the time of sampling.
c. Laboratory work done on analog fluid samples was also validated through the application of a robust workflow originally proposed by Professor William D. McCain, Jr. at Texas A&M University. In this approach, laboratory data is compared against reliable fluid property correlations, such as those in McCain *et al* [2011]. Agreement was observed, indicating that the laboratory work was valid.
d. The resulting fluid model was a black-oil variable bubble point model, in which internal consistencies of gas and oil properties were checked by ensuring that the oil compressibility (c_o) remained positive throughout the range of extrapolated pressures.
e. Five hydraulic flow units (named *HFU1* through *HFU5*) were identified from core samples spanned along more than 800 ft. This analysis was done in an objective

manner by use of hierarchical cluster analysis. The implementation was done in the form of a MATLAB code. The algorithm automatically determined the optimum number of flow units and their associated *FZI* values.

f. The hydraulic flow units (*HFU*) were associated rock-fluid properties, such as relative permeability and capillary pressure, obtained from experimental analysis. Consistency was observed, for example, it was noted that as rock quality increases from *HFU1* to *HFU5*, S_{wir} monotonically decreased and relative permeability end points monotonically increased.

g. Major sedimentological features were recognized for each flow unit. For instance, *HFU1* corresponded, in general, to intercalated claystones and siltstones, and for all practical purposes, it acts as a flow baffle or flow barrier.

4.2 Recommendations

a. Automatic outlier detection could be implemented in the MATLAB code for hierarchical cluster analysis of hydraulic flow units.

b. Incorporate a piece of code to automatically determine the change of slope in the elbow method (**Figure 3.6**).

c. Study the applicability of model-based cluster analysis, such as the expectation-maximization (EM) algorithm, as an alternative way to define hydraulic flow units.

REFERENCES

Abbaszadeh, M., Fujii, H., and Fujimoto, F. 1996. Permeability Prediction by Hydraulic Flow Units - Theory and Applications. Society of Petroleum Engineers. doi:10.2118/30158-PA.

Amaefule, J.O., Altunbay, M., and Tiab, D. 1993. Enhanced Reservoir Description: Using Core and Log Data to Identify Hydraulic (Flow) Units and Predict Permeability in Uncored Intervals/Wells. Presented at the 68th Annual Technical Conference and Exhibition of the Society of Petroleum Engineers, Houston, Texas, 03—06 October. SPE-26436. http://dx.doi.org/10.2118/26436.

Archer, J. and Wall, C. 1986. Petroleum Engineering: Principles and Practice. London: Graham & Trotman.

Baker, R.O., Yarranton, H.W. and Jensen, J.L. 2015. Practical reservoir engineering and characterization. Waltham, MA: Gulf Professional Publishing is an imprint of Elsevier.

Bear, J., 1972. Dynamics of Fluids in Porous Media. Elsevier, New York.

Blunt, M. 2017. Multiphase Flow in Permeable Media: a Pore-Scale Perspective. Cambridge, United Kingdom New York, NY: Cambridge University Press.

Bruno, I.A., Yanosik, I.L., and Tierney, I.W. 1972. Distillation Calculations with Nonideal Mixtures. In Extractive and Aziotropic Distillation. Advances in Chemistry Series 115, ACS, Washington, DC.

Cannon, S. 2018. Reservoir Modelling: a Practical Guide. Hoboken, NJ: Wiley.

Carman, P. C. 1961. L'e'coulement des Gaz a´ Travers les Milieux Poreux: Bibliothe'que des Sciences et Techniques Nucle'aires: Presses Universitaires de France.

Dandekar, A.Y. 2013. Petroleum Reservoir Rock and Fluid Properties. Boca Raton, FL: CRC Press.

Dake, L. P. 1978. Fundamentals of reservoir engineering. Amsterdam; New York; New York: Elsevier Scientific Pub. Co.; Distributors for the U.S. and Canada Elsevier North-Holland.

Dezfoolian, M., Riahi, M.and Kadkhodaie, A. 2013. Conversion of 3D seismic attributes to reservoir hydraulic flow units using a neural network approach: An example from the Kangan and Dalan carbonate reservoirs, the world's largest non-associated gas reservoirs, near the Persian Gulf. Earth Sciences Research Journal. 17. 75-85.

Dikkers, A. 1985. Geology in Petroleum Production: a Primer in Production Geology. Amsterdam New York: Elsevier.

Ebanks W.J. 1987. Flow Unit Concept — Integrated Approach to Reservoir Description for Engineering Projects (abs.). American Association of Petroleum Geologists Bulletin 71, 551–552.

Ebanks, W. J. 1992. Flow Units for Reservoir Characterization. Development Geology Reference Manual. AAPG Methods in Exploration Series no. 10, 1992. p. 282.285.

Han, J., Kamber, M. and Pei, J. 2012. Data Mining: Concepts and Techniques. Amsterdam; Boston: Elsevier/Morgan Kaufmann.

Hoffman, A. E., Crump, J. S., and Hocott, C. R. 1953. Equilibrium Constants for a Gas-Condensate System. Society of Petroleum Engineers. doi:10.2118/219-G.

Lake, L.W., Johns, R., Rossen, B. and Pope, G. 2014. Fundamentals of enhanced oil recovery. Richardson, Tex.: Society of Petroleum Engineers.

Land, C. 1967. Calculation of Imbibition Relative Permeability for Two- and Three Phase Flow From Rock Properties. Presented at the SPE 42nd Annual Fall Meeting, Houston, Texas, 01—04 October. SPE-1942. http://dx.doi.org/10.2118/1942.

Land, C. 1971. Comparison of Calculated with Experimental Imbibition Relative Permeability. Presented at the SPE Rocky Mountain Regional Meeting, Houston, Texas, 02—04 June. SPE-1942. http://dx.doi.org/10.2118/1942.

McCain, W.D. 1990. The Properties of Petroleum Fluids, second edition. PennWell.

McCain, W. D. and Spivey, J. P. 1999. Extrapolation of Laboratory Measured Black Oil and Solution Gas Fluid Properties for Variable Bubble Point Simulation. Society of Petroleum Engineers. doi:10.2118/56746-MS.

McCain, W.D., Spivey, J., and Lenn, C.P. 2011. Petroleum Reservoir Fluid Property Correlations, first edition. Tulsa, Oklahoma: PennWell.

McCain, W.D. 2016. Careful Sampling – Why Do We Care? [Class handout]. College Station, Texas: Texas A&M University, PETE-605.

McCain, W.D. (2018, January 8). Personal communication.

Pedersen, K.S., Christensen, P.L., and Shaikh, J.A. 2015. Phase Behavior of Petroleum Reservoir Fluids, second edition. CRC Press.

Satter, A., Iqbal, G.M. and Buchwalter, J.L. 2008. Practical enhanced reservoir engineering: assisted with simulation software. Tulsa, Okla.: PennWell Corp.

Schlumberger. 2015. ECLIPSE Reference Manual 2015.1. Schlumberger Information Solutions, Houston.

Schön, J. 2011. Physical Properties of Rocks: a Workbook. Amsterdam: Elsevier.

Slider, H.C. 1983. Worldwide Practical Petroleum Reservoir Engineering Methods: PennWell Books.

SPE. 2018. Petrowiki by Society of Petroleum Engineers (SPE). Relative Permeability Models, http://petrowiki.org/Relative_permeability_models (accessed 15 February 2018).

Spiteri, E. J., Juanes, R., Blunt, M. J., and Orr, F. M. 2008. A New Model of Trapping and Relative Permeability Hysteresis for All Wettability Characteristics. Society of Petroleum Engineers. doi:10.2118/96448-PA.

Stolz, A.-K., and Graves, R. M. 2003. Sensitivity Study of Flow Unit Definition by Use of Reservoir Simulation. Society of Petroleum Engineers. doi:10.2118/84277-MS.

Svirsky, D., Ryazanov, A., Pankov, M., Corbett, P. W. M., and Posysoev, A. 2004. Hydraulic Flow Units Resolve Reservoir Description Challenges in a Siberian Oil Field. Society of Petroleum Engineers. doi:10.2118/87056-MS.

Tiab, D. and Donaldson, E.C. 2016. Petrophysics: Theory and Practice of Measuring Reservoir Rock and Fluid Transport Properties, fourth edition. Amsterdam: Gulf Professional Publishing, an imprint of Elsevier.

van Golf-Racht, T.D. 1982. Fundamentals of fractured reservoir engineering. Amsterdam; New York: Elsevier.

Wattenbarger, R.A. 2000. Repressuring with Variable Bubble Point [Class handout]. College Station, Texas: Texas A&M University, PETE-611.

Zeus OL Peru SAC. 2016. Sedimentological descriptions. Unpublished internal document.

APPENDIX A

This appendix reproduces relevant fluid property correlations in McCain *et al* [2011]. Oil density at pressures equal or less than the bubble point are calculated from **Equations A.1** through **A.6** (McCain *et al* [2011]):

$$\rho_{oR} = \left[\frac{R_S\,\gamma_g + 4600\,\gamma_{STO}}{73.71 + {R_S\,\gamma_g}/{\rho_a}}\right] + \Delta\rho_p - \Delta\rho_T \tag{A.1}$$

$$\rho_a = a_0 + a_1\gamma_{gSP} + a_2\gamma_{gSP}\rho_{po} + a_3\gamma_{gSP}\rho_{po}^2 + a_4\rho_{po} + a_5\rho_{po}^2 \tag{A.2}$$

$$\Delta\rho_p = \frac{\left[0.167 + 16.181\left(10^{-0.0425\rho_{po}}\right)\right]}{\left(\frac{1000}{P}\right)} - 0.01\left[0.299 + 263\left(10^{-0.0603\rho_{po}}\right)\right]\left(\frac{P}{1000}\right)^2 \tag{A.3}$$

$$\Delta\rho_T = \frac{\left(0.00302 + \frac{1.505}{\left(\rho_{po}+\Delta\rho_p\right)^{0.951}}\right)}{(T-60)^{-0.938}} - \frac{\left[0.0216 - \frac{0.0233}{\left(10^{-0.0161\left(\rho_{po}+\Delta\rho_p\right)}\right)}\right]}{(T-60)^{-0.475}} \tag{A.4}$$

Where γ_{STO} is the stock-tank oil specific gravity; ρ_a is an apparent liquid density, and $\Delta\rho_p$ and $\Delta\rho_T$ are pressure and temperature corrections.

In **Equation A.2** coefficients are as follows: a_0 = -49.8930; a_1 = 85.0149; a_2 = -3.70373; a_3 = 0.0479818; a_4 = 2.98914; a_5 = -0.0356888.

Equations A.1 through **A.4** require iteration on ρ_{po}, for which the first trial value is given as:

$$\rho_{po} = 52.8 - 0.01R_s \tag{A.5}$$

At pressures greater than the bubble point, the oil density is found from the oil compressibility:

$$\rho_{oR} = \rho_{oRb} \cdot e^{[C_{ofb}(P-Pb)]} \quad \text{(A.6)}$$

Where ρ_{oRb} is the oil density at the bubble point, and Co_{fb} is the coefficient of isothermal compressibility of oil at pressures greater than the bubble point. Co_{fb} is found from equation 3.13 in McCain *et al* [2011].

The bubble point pressure (P_b) at a given reservoir temperature (T_R) and at a specified solution gas-oil ratio at the bubble point (R_{SB}) is calculated from **Equations A.7** through **A.9**:

$$ln(P_B) = 7.475 + 0.713Z + 0.0075Z^2 \quad \text{(A.7)}$$

$$Z = \sum_{n=1}^{4} Z_n \quad \text{(A.8)}$$

$$Z_n = C0_n + C1_n VAR_n + C2_n VAR_n^2 + C3_n VAR_n^3 \quad \text{(A.9)}$$

Coefficients C0, C1, C2 and C3 for the *n* variables *VAR* are given in **Table A.1**:

Table A.1 Coefficients in the correlation for P_b (after McCain *et al* [2011])

n	*VAR*	$C0_n$	$C1_n$	$C2_n$	$C3_n$
1	$\ln(R_{SB})$	-5.48	-0.0378	0.281	-0.0206
2	API	1.27	-0.0449	4.36×10^{-4}	-4.76×10^{-6}
3	γ_{gSP}	4.51	-10.84	8.39	-2.34
4	T_R	-0.7835	6.23×10^{-3}	-1.22×10^{-5}	1.03×10^{-8}

The solution gas-oil ratio (R_S) at reservoir pressures lower than P_B is calculated from **Equations A.10** through **A.13**:

$$R_S = R_{SB}\left\{a_1\left(\frac{P-14.7}{P_b-14.7}\right)^{a_2} + (1-a_1)\left(\frac{P-14.7}{P_b-14.7}\right)^{a_3}\right\} \quad \text{(A.10)}$$

$$a_1 = A_0\left(\gamma_{gSP}\right)^{A_1} API^{A_2} T^{A_3} (P_B - 14.7)^{A_4} \quad \text{(A.11)}$$

$$a_2 = B_0\left(\gamma_{gSP}\right)^{B_1} API^{B_2} T^{B_3} (P_B - 14.7)^{B_4} \quad \text{(A.12)}$$

$$a_1 = C_0\left(\gamma_{gSP}\right)^{C_1} API^{C_2} T^{C_3} (P_B - 14.7)^{C_4} \quad \text{(A.13)}$$

Coefficients in **Equations A.10** through **A.13** are given in **Table A.2**.

Table A.2 Coefficients in the correlation for *Rs* below P_b (after McCain *et al* [2011])

n	A_n	B_n	C_n
0	9.73×10^{-7}	0.022339	0.725167
1	1.672608	-1.004750	-1.485480
2	0.929870	0.337711	-0.164741
3	0.247235	0.132795	-0.091330
4	1.056052	0.302065	0.047094

The coefficient of isothermal compressibility of oil at reservoir pressures greater than bubble point pressure (C_{ofb}) is calculated from **Equations A.14** through **A.16**:

$$ln\left(C_{ofb}\right) = 2.434 + 0.475Z + 0.048Z^2 - ln(10^6) \quad \text{(A.14)}$$

$$Z = \sum_{n=1}^{6} Z_n \quad \text{(A.15)}$$

$$Z_n = C0_n + C1_n VAR_n + C2_n VAR_n^2 \quad \text{(A.16)}$$

Coefficients in **Equations A.14** through **A.16** for the *n* variables *VAR* are in **Table A.3**:

Table A.3 Coefficients in the correlation for P_b (after McCain *et al* [2011])

n	*VAR*	$C0_n$	$C1_n$	$C2_n$
1	ln(API)	3.011	-2.6254	0.497
2	$\ln(\gamma_{gSP})$	-0.0835	-0.259	0.382
3	$\ln(P_b)$	3.51	-0.0289	-0.0584
4	$\ln(P/P_b)$	0.327	-0.608	0.0911
5	$\ln(Rs_b)$	-1.918	-0.642	0.154
6	$\ln(T_R)$	2.52	-2.73	0.429

The oil formation volume factor at reservoir pressures equal to and less than P_B (B_o) is found from **Equation 2.3**. At pressures greater than P_B, B_o is given by **Equation A.17**:

$$B_o = B_{ob} \cdot e^{[C_{ofb}(P-Pb)]} \tag{A.17}$$

Equation A.17 is not a correlation. It follow directly from the definition of the coefficient of isothermal compressibility of oil.